remote sensing

MDPI

Article

Airborne Validation of ICESat-2 ATLAS Data over Crevassed Surfaces and Other Complex Glacial Environments: Results from Experiments of Laser Altimeter and Kinematic GPS Data Collection from a Helicopter over a Surging Arctic Glacier (Negribreen, Svalbard)

Ute C. Herzfeld [1,*], Matthew Lawson [1], Thomas Trantow [1] and Thomas Nylen [2]

[1] Geomathematics, Remote Sensing and Cryospheric Sciences Laboratory, Department of Electrical, Computer and Energy Engineering University of Colorado Boulder, Boulder, CO 80309-0574, USA; Matthew.Lawson@colorado.edu (M.L.); Thomas.Trantow@colorado.edu (T.T.)

[2] DTU Space, Danish Technical University (DTU), Elektrovej, Building 328, Kgs, 2800 Lyngby, Denmark; thony@space.dtu.dk

* Correspondence: ute.herzfeld@colorado.edu

check for updates

Citation: Herzfeld, U.C.; Lawson, M.; Trantow, T.; Nylen, T. Airborne Validation of ICESat-2 ATLAS Data over Crevassed Surfaces and Other Complex Glacial Environments: Results from Experiments of Laser Altimeter and Kinematic GPS Data Collection from a Helicopter over a Surging Arctic Glacier (Negribreen, Svalbard). *Remote Sens.* **2022**, *14*, 1185. https://doi.org/10.3390/rs14051185

Academic Editors: Shridhar Jawak, Andreas Kääb, Veijo Pohjola, Hiroyuki Enomoto, Geir Moholdt, Kjell Arild Høgda, Małgorzata Błaszczyk, Bo N. Andersen, Ann Mari Fjæraa, Bartłomiej Luks, Roberto Salzano and Frode Dinessen

Received: 4 October 2021
Accepted: 30 January 2022
Published: 27 February 2022

Publisher's Note: MDPI stays neutral with regard to jurisdictional claims in published maps and institutional affiliations.

Copyright: © 2022 by the authors. Licensee MDPI, Basel, Switzerland. This article is an open access article distributed under the terms and conditions of the Creative Commons Attribution (CC BY) license (https://creativecommons.org/licenses/by/4.0/).

Abstract: The topic of this paper is the airborne evaluation of ICESat-2 Advanced Topographic Laser Altimeter System (ATLAS) measurement capabilities and surface-height-determination over crevassed glacial terrain, with a focus on the geodetical accuracy of geophysical data collected from a helicopter. To obtain surface heights over crevassed and otherwise complex ice surface, ICESat-2 data are analyzed using the density-dimension algorithm for ice surfaces (DDA-ice), which yields surface heights at the nominal 0.7 m along-track spacing of ATLAS data. As the result of an ongoing surge, Negribreen, Svalbard, provided an ideal situation for the validation objectives in 2018 and 2019, because many different crevasse types and morphologically complex ice surfaces existed in close proximity. Airborne geophysical data, including laser altimeter data (profilometer data at 905 nm frequency), differential Global Positioning System (GPS), Inertial Measurement Unit (IMU) data, on-board-time-lapse imagery and photographs, were collected during two campaigns in summers of 2018 and 2019. Airborne experiment setup, geodetical correction and data processing steps are described here. To date, there is relatively little knowledge of the geodetical accuracy that can be obtained from kinematic data collection from a helicopter. Our study finds that (1) Kinematic GPS data collection with correction in post-processing yields higher accuracies than Real-Time-Kinematic (RTK) data collection. (2) Processing of only the rover data using the Natural Resources Canada Spatial Reference System Precise Point Positioning (CSRS-PPP) software is sufficiently accurate for the sub-satellite validation purpose. (3) Distances between ICESat-2 ground tracks and airborne ground tracks were generally better than 25 m, while distance between predicted and actual ICESat-2 ground track was on the order of 9 m, which allows direct comparison of ice-surface heights and spatial statistical characteristics of crevasses from the satellite and airborne measurements. (4) The Lasertech Universal Laser System (ULS), operated at up to 300 m above ground level, yields full return frequency (400 Hz) and 0.06–0.08 m on-ice along-track spacing of height measurements. (5) Cross-over differences of airborne laser altimeter data are -0.172 ± 2.564 m along straight paths, which implies a precision of approximately 2.6 m for ICESat-2 validation experiments in crevassed terrain. (6) In summary, the comparatively light-weight experiment setup of a suite of small survey equipment mounted on a Eurocopter (Helicopter AS-350) and kinematic GPS data analyzed in post-processing using CSRS-PPP leads to high accuracy repeats of the ICESat-2 tracks. The technical results (1)–(6) indicate that direct comparison of ice-surface heights and crevasse depths from the ICESat-2 and airborne laser altimeter data is warranted. Numerical evaluation of height comparisons utilizes spatial surface roughness measures. The final result of the validation is that ICESat-2 ATLAS data, analyzed with the DDA-ice, facilitate surface-height determination over crevassed terrain, in good agreement with airborne data, including spatial characteristics, such as surface roughness, crevasse spacing and depth, which are key informants on the deformation and dynamics of a glacier during surge.

Keywords: ICESat-2; laser altimetry; kinematic GPS experiments; glaciology; surge glaciers; svalbard; density dimension algorithm for ice surfaces; airborne validation of satellite data

1. Introduction

With the Advanced Topographic Laser Altimeter System (ATLAS), NASA's ICESat-2, launched on 15 September 2018, carries the first space-borne multi-beam micro-pulse photon-counting laser altimeter system [1,2]. The ATLAS system records returns from every single photon in the 532 nm range of the sensor, which facilitates determination of along-track surface heights at the 0.7 m resolution of the sensor (under clear-sky atmospheric conditions), using the Density Dimension Algorithm for ice surfaces (DDA-ice) [3]. This capability of high-density measurements constitutes a better than 200-fold improvement in resolution over the 173-m spacing of the Geoscience Laser Altimeter System (GLAS) of the ICESat Mission, which operated from 2003 to 2009 [4,5].

Such increased density of measurements requires a field validation with high geodetical accuracy to establish that the surface heights determined from ICESat-2 accurately represent the actual surface heights and morphologies of an ice surface, especially for the complex morphology of heavily crevassed ice surfaces. Capturing crevassed surfaces accurately is important, because crevassing occurs as a sign of fast-moving and accelerating glaciers. Glacial acceleration is one of the largest sources of uncertainty in sea-level-rise assessment, according to the Fifth Assessment Report (AR5) of the Intergovernmental Panel of Climate Change (IPCC) [6]. The different spatial characteristics of crevasse fields, including crevasse spacing, depth and surface roughness, yield information on the deformation characteristics and ice dynamics during glacial acceleration [7–11].

To assess the surface-height determination capabilities of ICESat-2 ATLAS, we carried out an airborne geophysical evaluation campaign over Negribreen, Svalbard, during surge in summer 2019. The objective of this paper is a geodetical and glaciological evaluation using laser altimeter, image and geodetical data collected during this campaign. Negribreen accelerated to more than 200 times its quiescent-phase ice speed in July 2017, with a maximal speed of 22 m/day at the height of the surge acceleration [3]. The glacier's rapid mass transfer to the Arctic Ocean during the surge provides a prime example of the relationship between dramatic mass loss through calving and the surge process [12]. A surge in a Svalbard glacier typically lasts 7–10 years [13]. Maximal velocities in summer 2019 were still around 7 = 6 m/day, based on our analysis of Sentinel-1 Synthetic Aperture Radar (SAR) data.

Negribreen during surge is an ideal validation region, because many types of crevasses and other complex surface types exist in close proximity (Figure 1). This heavily crevassed environment provides a set of challenges for surface-height measurement and surface-height determination, whose solution will indicate that surface heights can be determined accurately in other crevassed and smooth glaciated regions as well. Because crevasses are relatively small features, a high geodetical accuracy and a close repeat of satellite track by airborne tracks is important, both will be analyzed in this paper. As there is not much literature about kinematic GPS data collection from a helicopter for the purpose of satellite data evaluation, the mathematical geodetical results of this paper are expected to be of use for future airborne experiments.

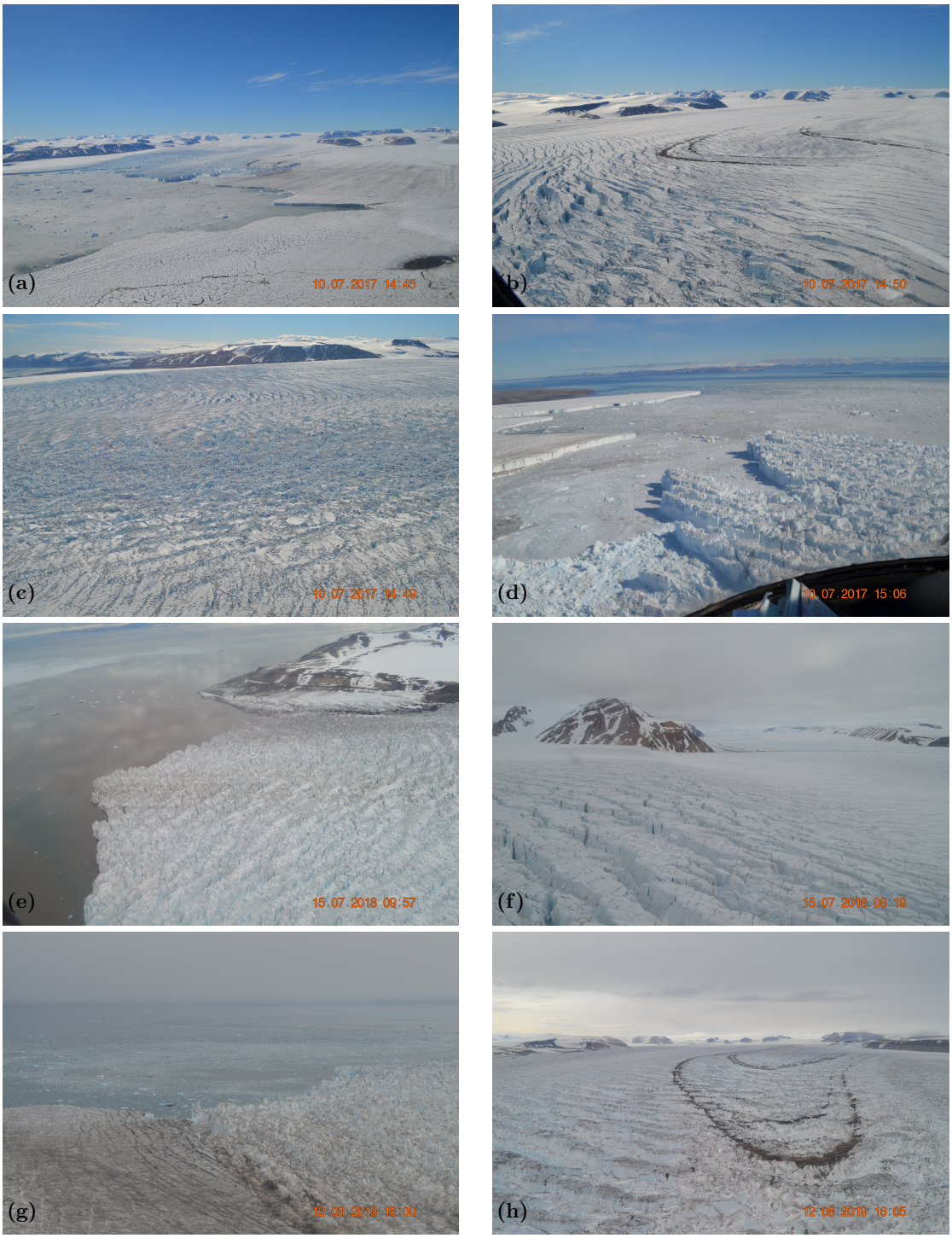

Figure 1. Negribreen during surge in 2017–2019. The multitude of different surface types indicates that a glacier during surge provides an ideal test situation for evaluation of height determination over crevassed and other complex ice surfaces. Photographs by Ute Herzfeld. (**a**) Negribreen surge July 2017, overview. (**b**) Wavy crevasses and folded moraines in central Negribreen, July 2017. (**c**) Several different crevasse provinces in central Negribreen, July 2017. (**d**) Calving front, ice fingers advancing into the ocean (front right), with smooth surface of non-surging Ordonannsbreen in the back left, July 2017. (**e**) Crevasse province near calving front July 2018. (**f**) Blocky crevasses near RGT 594 region, July 2018. (**g**) Ordonannsbreen-Negribreen boundary near calving front, August 2019. (**h**) Folded moraines and surge crevasses, August 2019.

The precision of ICESat-2 ATL06 (version 003) [14,15] ice surface height data has been determined as better than 7.2 cm, with a bias of less than 3.3 cm for smooth and flat ice/snow surfaces at 88° Southern latitude in Antarctica, which is the circle of convergence of the ICESat-2 ground tracks [16]. Ref [17] conducted a field evaluation along the Chinese Antarctic Expedition Route (CHINARE, a route driven with a Pisten Bully) near Amery Ice Shelf, using GNSS, in December 2019 to February 2020, finding that ICESat-2 ATL06 (version 003 data) are precise to 1.5 cm with 9.1 cm precision and surface heights of ATL03 photon events [18,19] are accurate to 4.3 cm with 8.5 cm precision. Since this is a route that was driven with a Pisten Bully, it is all smooth, uncrevassed ice. However, the ICESat-2 ATL06 data product is a 40 m along-track ice-surface height product with 20 m postings, which generally does not report crevassed and otherwise morphologically complex glaciated terrain, and the photon classification on the ATL03 product often fails over such terrain [3]. The study in this paper complements such determinations of measurement accuracy over smooth and flat ice surfaces by investigations of surface-height determination over crevassed and otherwise complex regions, derived using the DDA-ice. The surface-height-determination problem has been addressed in [3], here, we focus on the geodetical component of ICESat-2 validation campaign data over crevassed terrain.

In this paper, we describe the ICESat-2 ATLAS data, experimental and instrumental setup of the airborne geophysical field campaigns, the process for geodetical correction of the airborne data using GPS/GNSS data and IMU data, and the resultant accuracies. Results will include (1) the capability to repeat satellite tracks during a helicopter-based airborne validation campaign, (2) the type of geodetical corrections and associated accuracy, (3) spatial characteristics of airborne data (on-ice spacing of resultant altimeter data), (4) determination of cross-over heights from airborne laser altimeter data after correction as an indicator of vertical precision of the field data, (5) the resultant accuracy of surface-height determination and variability, derived from ICESat-2 ATLAS data using the DDA-ice, and (6) the resultant ability to derive spatial characterizations of the morphological properties of the ice surface, exemplified by a surface-roughness parameter.

2. ICESat-2 ATLAS Data

2.1. ATLAS Instrumentation, Data Collection Geometry, Basic Corrections and ATL03 Data Product

ICESat-2 ATLAS data are collected along-track, for 3 pairs of 2 beams, a strong beam and a weak beam per pair, where the weak beam has a quarter of the energy of the strong beam [1,2]. Across-track separation of the beams on the Earth's surface is 3.3 km between the centers of adjacent pairs and 90 m for the beams within each pair; ICESat-2 beam pattern and track geometry are illustrated in Figure 2. The sensor operates in the 532 nm wavelength (green light) with a pulse-repetition rate (PRF) of 10 kHz. The PRF results in a nominal 0.7 m spacing of the laser pulses on the Earth's surface, under clear-sky atmospheric conditions. ATLAS has a footprint diameter of less than 17.4 m at 85% encircled energy. The Field of View (FOV) of the receiver telescope is 83.8 µrad, equivalent to 45 m FOV on the surface of the Earth. Observatory performance has been assessed in [20], where the actual footprint is characterized as closer to 10 m in diameter. As the FOV moves along the satellite ground track and returns from every single photon (in the 532 nm wavelength domain of the sensor) are recorded, surface structures at much higher resolution than footprint diameter can be resolved (see Section 2.2 and [3]). The instrumentation and derivation of the recorded photon point cloud are described in [2], and any technical component of the instrument and data set necessary for understanding the work in this paper is found in [3].

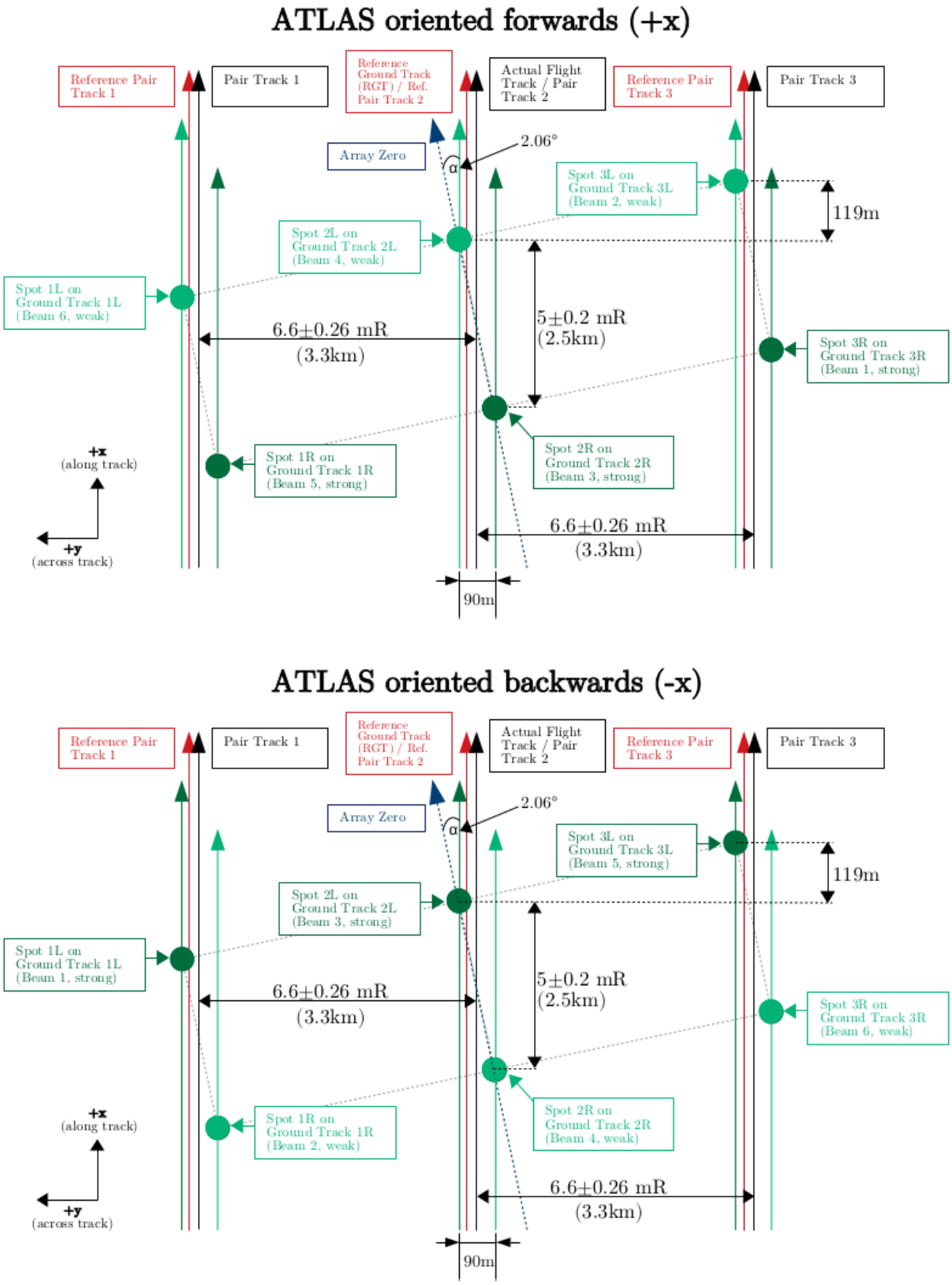

Figure 2. ICESat-2 beam pattern and track geometry. For observatory orientations of ATLAS flying forward ("weak beams leading") and ATLAS flying backward ("strong beams leading"). Beam numbering is a feature of the transmitter array, while spot and ground track numbering is a feature of the ATLAS data products, see Table 1. (Figure from [3], Figure 3).

ATLAS records returns from every photon in the 532 nm wavelength domain of the sensor. This results in a so-called photon point cloud. The photon point cloud includes photon events from ambient light (background) and photon events that results from the active laser signal of the instrument; these types of photons are initially not distinguishable. Classification of photons into signal and background requires a sophisticated mathematical algorithm, since the classification problem is mathematically ill-posed. For the solution of the classification problem and the determination of surface heights, we apply the density-dimension algorithm for ice surfaces, the DDA-ice [3,21], briefly introduced in Section 2.2. Data in this paper stem from the ICESat-2 ATL03 data product (version 003) [19], described fully in the Algorithm Theoretical Base Document (ATBD) for Geolocated Photon Points [18]. There is a classification of photons provided on ATL03, however, the work in our paper utilizes the classification based on the DDA-ice (the ATL03 classification often fails over crevassed surfaces). Note that technically, the data sets (ICESat-2 ATLAS data products) are referred to by version number (here: version 3), while the algorithms used to create the data products are referred to by release number (here: release 3). Because the geodetical corrections have not changed significantly in a way that would affect the ATL03 data geolocation and especially the representation of crevasse characteristics, the field validation presented in this paper is expected to be valid for subsequent releases as well (to release 5, the last release at publication date of this paper) [22].

Of relevance for the airborne validation campaign of the ICESat-2 ATLAS data is the concept of Reference Ground Tracks (RGTs). ATLAS ground tracks are referenced to the RGTs, which are calculated ahead of time, prior to the mission. There are a total of 1392 RGTs. Actual ATLAS ground tracks are derived after data collection and following detailed geolocation.

The ICESat-2 beam pattern and track geometry depend on the orientation of the observatory, which can be flown in two modes, forwards (+x) and backwards (−x) (Figure 2). All data in this paper were collected during an "ATLAS oriented backwards" phase in July and August 2019. The orientation of the observatory changes which ground track stems from a weak beam and which one from a strong beam (see, Table 1). Therefore, for each track used in this paper "strong beam" or "weak beam" are specified (tracks are labeled gt1r, gt1l, gt2r, gt2l, gt3r, gt3l where the number stands for the beam and the letter for "left" or "right". Beam 2 is the center beam and the RGT splits the distance between gt2r and gt2l by design. Reference pair tracks split the distance between (gt1r, gt1l) and (gt3r, gt3l). Both weak beam and strong beam data were evaluated during our validation campaign. For shortness, we use the terminology "predicted ATLAS tracks" for ground tracks calculated ahead of time from the RGTs and "actual ATLAS tracks" for ground tracks derived from ATLAS observations, corrected as summarized in the next paragraph.

After data collection, the geolocation process results in the association of latitude, longitude and height for each telemetered photon event in the point cloud. It uses Precision Pointing Determination (PPD) of the laser and Precision Orbit Determination (POD). ATLAS carries a Laser Reference System (LRS), two GPS antennas and Spacecraft Star Trackers. The process is described in short in [3], in more detail in [2] and in full in the geodetical part of the ATL03 ATBD for Receive Photon Geolocation ATL03g [22], see also [23]. The location of the "bounce point" of the laser altimeter on the ice surface is given in the International Terrestrial Reference Frame (ITRF, Petit and Luzum [24]) ITRF 2014 (ITRF14) as latitude, longitude and height w.r.t. the World Geodetical System WGS84 in realization G1150 with ellipsoid constants (a_e = 6,378,137 m, $\frac{1}{f} = 298.257223563$) [2]. We will utilize the same referencing for the airborne laser altimeter data of our campaign. After geolocation, several geophysical corrections are applied to the photon points [2,3].

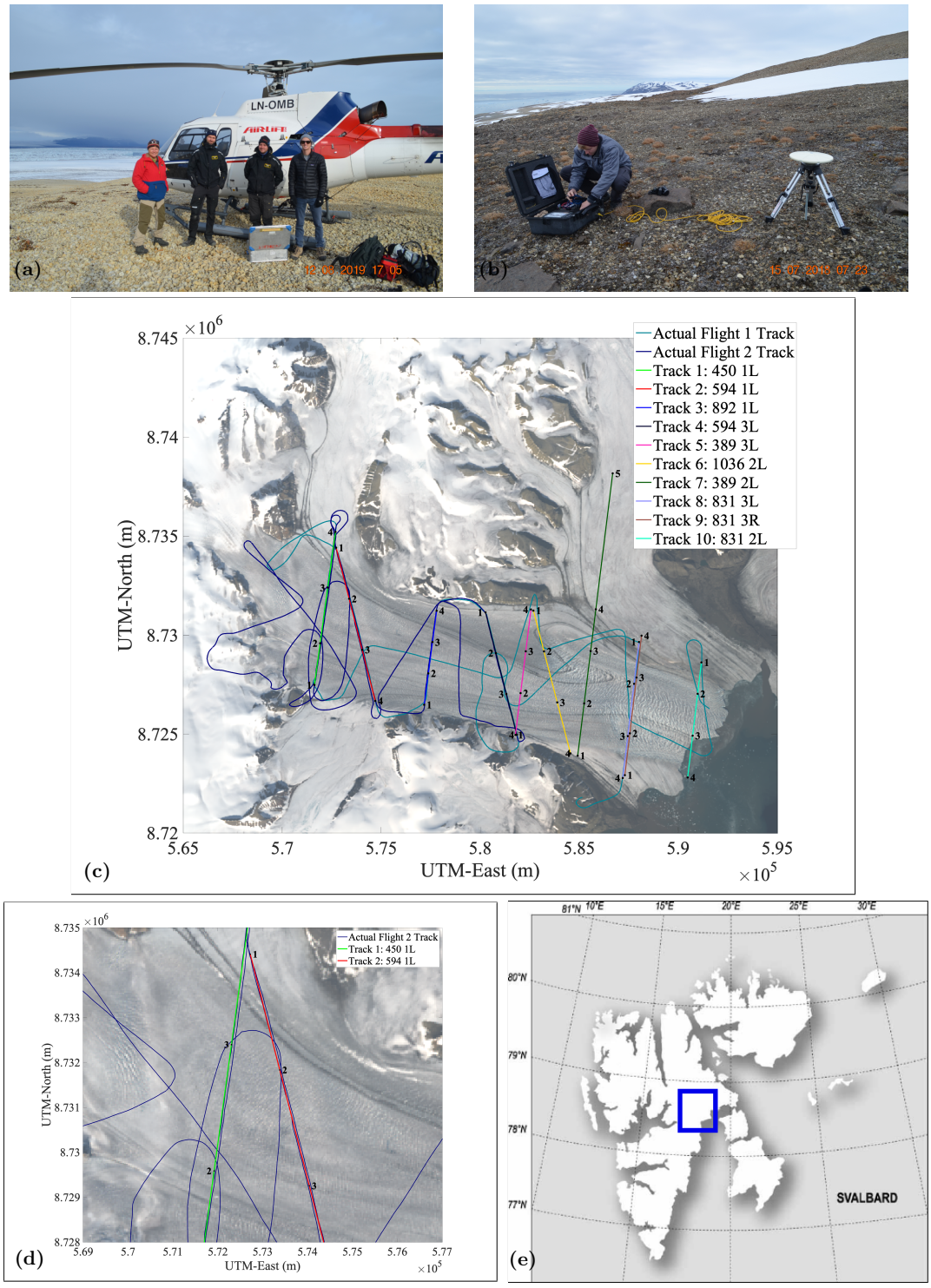

Figure 3. Negribreen ICESat-2 Airborne Validation Campaign 2019: Experiment setup, track maps, location map and satellite image. (**a**) Field team 2019 (f.l.t.r. Ute Herzfeld, Harald Sandal (pilot) and Gustav Svanström (technician), Matthew Lawson, in front of the Airlift/ NPI helicopter; photograph by Thomas Trantow), on the side of Negribreen, flight 1, 12 August 2019, (**b**) GPS base station on a ridge above Negribreen, 2018 (Connor Myers), photograph by Ute Herzfeld. (**c**) Planned and actual flight tracks and predicted ICESat-2 ATLAS ground tracks. Flight 1, 12 August 2019; Flight 2: 13 August 2019. Background Landsat-8 data (5 August 2019) [LC08_L1TP_215003_20190805_20190820_01_T1]. (**d**) Zoom into (**c**) for area of RGT 594 and RGT 450 analyzed in this paper. (**e**) Location map. (Figure panels (**c**–**e**) after [3]).

Table 1. Identifiers for ATLAS orientations. (After [3], Table 1).

ATLAS Flying Forwards							
PCE	**Strength**	**ATLAS Spot**	**Pair**	**GT**	**ATL03 Beam**	**ATL04/09 Atmosphere**	**Orientation**
1	Strong	1	Right	gt3r	5	profile_3	1
1	Weak	2	Left	gt3l	6	profile_3	1
2	Strong	3	Right	gt2r	3	profile_2	1
2	Weak	4	Left	gt2l	4	profile_2	1
3	Strong	5	Right	gt1r	1	profile_1	1
3	Weak	6	Left	gt1l	2	profile_1	1
ATLAS Flying Backwards							
PCE	**Strength**	**ATLAS Spot**	**Pair**	**GT**	**ATL03 Beam**	**ATL04/09 Atmosphere**	**Orientation**
1	Strong	1	Right	gt1l	5	profile_1	0
1	Weak	2	Left	gt1r	6	profile_1	0
2	Strong	3	Right	gt2l	3	profile_2	0
2	Weak	4	Left	gt2r	4	profile_2	0
3	Strong	5	Right	gt3l	1	profile_3	0
3	Weak	6	Left	gt3r	2	profile_3	0

2.2. The Density-Dimension Algorithm for Ice-Surface-Height Determination (DDA-Ice) in Crevassed and Other Complex Terrain—Description in a Nutshell

The analysis of the ATLAS data utilizes the Density-Dimension Algorithm for ice surfaces (DDA-ice) [3,21]. The DDA-ice is an algorithm specifically developed for surface-height determination from micro-pulse photon-counting laser altimeter data, especially those of the ICESat-2 ATLAS instrument and similar sensors. The DDA-ice is introduced in [21] for data from the Slope Imaging Multi-polarization Photon-counting Lidar (SIMPL) [25,26], an airborne micro-pulse photon-counting laser altimeter system that was employed as an ICESat-2 predecessor instrument in test flights, and has been first applied to ICESat-2 ATLAS data in [3]. The data from the ATLAS instrument have the form of a point cloud of geolocated photons [2]. The DDA-ice utilizes a Gaussian radial basis function (*rbf*) for data aggregation. The *rbf* is evaluated for every single photon in the point cloud; this operation results in a density field. In the next step, an auto-adaptive threshold function is applied to separate signal and background photons; this function automatically adapts to the different background properties of daytime, twilight and nighttime, apparent surface reflectivity (ASR) and some instrument characteristics, such as the afterpulse of the lidar signal. The algorithm is termed density-dimension algorithm, because density is used as an additional dimension in the signal-background classification step. The resultant surface heights have the same resolution as the sensor, which is nominally 0.7 m along-track under clear-sky atmospheric conditions. The DDA-ice uses its own cloud flag algorithm (it does not rely on the cloud flag in the atmospheric data product ATL04 [27,28]). The last step of the DDA-ice is the ground follower. The ground follower is a piece-wise linear interpolator, whose segmentation automatically adapts to surface roughness, resulting in 2.5 m spacing for crevassed (or generally, rough) surfaces and 5 m for uncrevassed (or generally, smooth) surfaces. The DDA-ice is controlled by a set of so-called algorithm-specific parameters, introduced to facilitate quick adjustment of the algorithm should the performance characteristics of the ATLAS lasers change. The values of the algorithm-specific parameters employed in the analysis in this study are given in Table 2. Input data for the DDA-ice are geolocated photons, as given in the publicly available ICESat-2 ATLAS data product ATL03 "Global Geolocated Photons", version 3 [19], described in Neumann et al. [2,29]. The

DDA-ice does not utilize the signal classification given in ATL03, but signal-background classification is an intrinsic step of the DDA-ice (for a comparison, see [3]).

Table 2. DDA-ice parameters. Strong beam, weak beam—ATLAS beams. Parameters are the same as used in [3], parameters used for strong beam are the same as parameters optimized for analysis of SIMPL_green (532nm parallel polarized) channels. Variables Q and S are now algorithm-specific parameters for DDA-ice. Resolution of the ground follower is 2.5 m over rough/ crevassed surfaces and 5 m over smooth surfaces. See also [21].

Symbol	Meaning	Strong Beam ATLAS (Actual)	Weak Beam ATLAS (Actual)
s	standard deviation (m)	3	4
u	cutoff (number of standard deviations)	1	1
a	anisotropy	1	1
q	threshold quantile	0.5	0.6
k	threshold bias offset	1	0.2
l	slab thickness (m)	200	200
R	resolution of ground follower (m)	5	5
r	factor to reduce the R parameter	2	1
-	resolution of ground follower for rough surfaces (m)	2.5	5
Q	crevasse depth quantile	0.5	0.5
S	standard deviation threshold of thresholded signal to trigger small step size in ground follower (m)	1.75	1.75

3. Experiment Setup for the Negribreen ICESat-2 Airborne Geophysical Validation Campaign

3.1. Geographic Region and Ice-Surface Types during Surge

The Negribreen Glacier System (NGS) is located on Spitsbergen in Svalbard, it forms an outlet of the Filchnerfønna ice cap (see, Figure 3). The calving front of Negribreen was located at approximately (78.573° N, 19.083° E) in 2019. An overview of main areas of the Negribreen Glacier System, including Negribreen (in center), Ordonnansbreen (the glacier that joins Negribreen close to the calving front) and Akademikerbreen (the glacier that joins upper Negribreen from the North) is seen in the background Landsat-8 image in Figure 3c.

Ice surface types during the surge include many different crevasse classes (Figure 1). Figure 1a shows smooth ice of Ordonannsbreen contrasting with the highly fractured ice of Negribreen, which calves into the bay, part of the Arctic Ocean. Wavy crevasses and folded moraines, the indicators that a glacier is a surge-type glacier, are seen in Figure 1b. Figure 1c illustrates several types of crevasse provinces, delineated from neighboring provinces by relatively clear boundaries. Heavily crevassed ice that advances rapidly into the Arctic Ocean indicates the rapid mass loss during the surge in July 2017 (Figure 1d) and July 2018 (Figure 1e). Figure 1f shows a typical surge crevasse type, characterized by blocky crevasses with subordinate, thin multidirectional crevasses in the region of RGT594. The surface of slow-moving Ordonannsbreen (left) is only crevassed near the boundary to surging Negribreen and otherwise smooth (Figure 1g). Lastly, Figure 1h presents a picture of multi-generational crevasses resultant from several deformation events in an area where the folded moraines exist, taken in August 2019. While maximal ice speeds during the height of acceleration in July 2017 reached 22 m per day, the region of crevassed ice expanded during the evolution of the surge and the maximal speeds decreased. Ice-surface velocity magnitudes derived from analysis of Sentinel-1 SAR data in August of 2019 were about 6 m (5.96 m) near the front of the glacier and 1–2 m in the region of the surveys

analyzed in this paper (Figure 4a). High-resolution satellite imagery from Planet SkySat, collected on 2019, August 18, illustrates the type of complex crevassing that exists near the ice front, in the fastest-moving region of the glacier, over 3 years after the start of the surge in spring 2016 (Figure 4b).

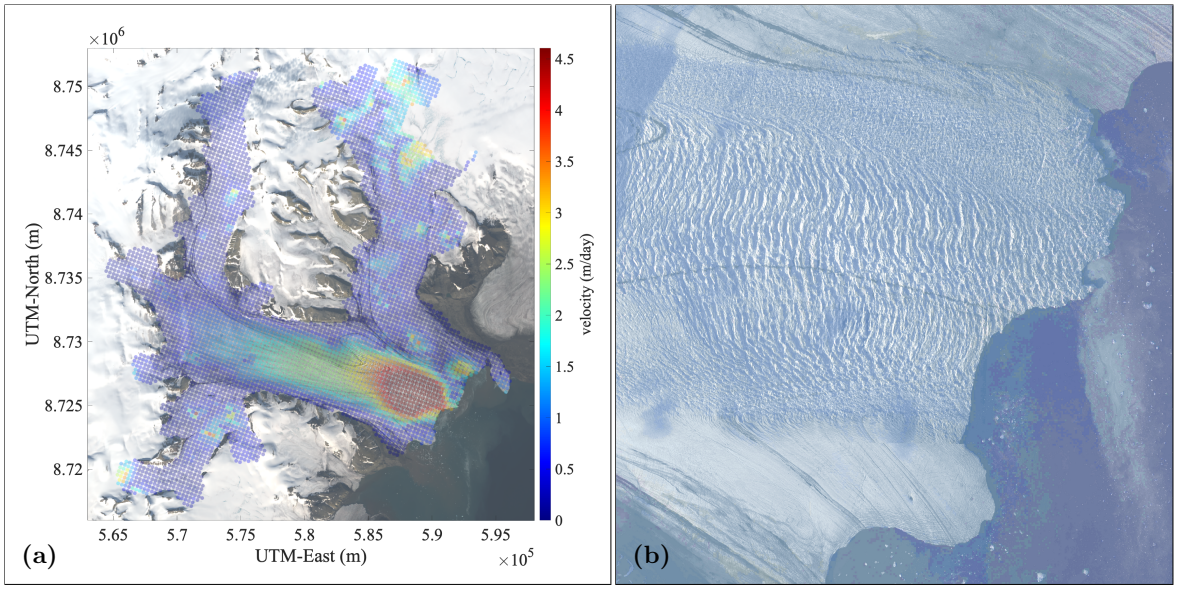

Figure 4. Negribreen velocity magnitude and crevassing at time of validation campaign in August 2019. (**a**) Velocity magnitude, calculated from ESA Copernicus Mission Sentinel-1 SAR data for 9 August 2019 to 21 August 2019. Highest velocity magnitude was 5.96 m/day near the calving front. (**b**) Crevasse types in the fastest-moving region near the front, Planet SkySat image, collected 18 August 2019. [20190818_150858_ssc9_u0002_panchromatic_dn.tif]. (Figure panel (**b**) after [3]).

3.2. Experiment Setup

We conducted airborne geophysical observation campaigns over Negribreen during surge in the summers of 2017, 2018 and 2019. The campaigns over Negribreen had two objectives, (1) study of the state of the surge in the Negribreen Glacier System and (2) validation of ICESat-2 data. The 2018 campaign was carried out in preparation of ICESat-2 validation, prior to launch of ICESat-2 (which was on 15 September 2018), while the 2019 campaign obtained synoptical airborne and satellite observations. Airborne data were collected from a helicopter (Eurocopter AS 350), operated by Airlift under the auspices of the Norwegian Polar Institute, chartered for our campaign by the University of Colorado Geomathematics Group (Figure 3a).

During the 2019 field validation campaign, airborne geophysical data were collected along predicted ICESat-2 ATLAS ground tracks (see, Figure 3c) on 12 August 2019 (Flight 1) and 13 August 2019 (Flight 2). The locations of ground tracks from our flight campaign are referred to as flight tracks, or flight ground tracks (with coordinates calculated as described in this paper). The analysis in this paper utilizes predicted ATLAS ground tracks, actual ATLAS ground tracks and flight ground tracks. A zoom into Figure 3c, seen in Figure 3d, shows the tracks along RGT 450 and RGT 594, which will be analyzed in this paper, their relative location and crevasse types surveyed. Planet SkySat satellite image data, specifically collected to support this project, provide additional information suitable for evaluation of ICESat-2 measurements. Figure 3f shows crevasse provinces near the calving front in a Planet SkySat image taken on 18 August 2019. Extensional wavy crevasses, indicative of the area of highest velocities at time of image capture, dominate the northern central part of Negribreen, north of the trace of a medial moraine in upstream Negribreen. The fast-moving region is flanked by shear crevasses in its north and south, then (in an outward direction from the center) more closely spaced crevasses in the north, followed by smooth, slow-moving ice provinces in the north and south.

3.3. Instrumentation

During the 2018 and 2019 airborne geophysical campaigns, we collected laser altimeter data and image data, which were geolocated using coincidently collected Global Positioning System (GPS) and Inertial Measurement Unit (IMU) data. The same instruments were used in both years, except for the GPS Rover, and included the following:

(1) *Laser altimetry:* Universal Laser System (ULS), LaserTech Inc. (Denver, Colorado, U.S.A.), mounted on helicopter (400 Hz data);
(2) *Global Positioning System (GPS) Receivers (Base and Rover):*
    (2.1) Kinematic GPS
        (2.1.1) GPS Base Station placed on the side of Negribreen (Trimble NetR9)
        (2.1.2) GPS Rover, mounted on a skid of helicopter (Septentrio APS-3G in 2018, Trimble R10 in 2019) (10 Hz data)
    (2.2) "Button GPS", a simple GPS system placed on the dashboard of the helicopter under the window (1 Hz data)
(3) *Attitude correction:* Inertial Measurement Unit (IMU), LORD 3DM-GX5-15 Vertical Reference Unit (mounted inside the helicopter, taped to the floor) (1 Hz data)
(4) *Nadir-pointed time-lapse imagery:* GoPro Hero5 Camera, mounted outside on the helicopter (2 Hz data)
(5) *Photographs:* Several handheld cameras (NIKON D5100 and other Nikon cameras)

(1) Laser Altimetry. The LaserTech ULS is a class-1, eye-safe laser that operates at 905 nm (Near-Infrared) with a configurable pulse-repetition frequency (PRF), set to 4000 Hz with 10-point averaging to yield an effective PRF of 400 Hz during the Negribreen campaigns. Beam divergence is 3 mrad, which results in a 30 cm footprint at 100 m range (see, Table 3). The ULS was integrated by members of the University of Colorado Geomathematics, Remote Sensing and Cryospheric Sciences Laboratory (the first three authors) for altimetry use from small manned and unmanned aircraft, utilizing a so-called engineering kit provided by LaserTech. An earlier integration is described in [30], for use aboard the NASA Sierra UAV during the Characterization of Arctic Sea Ice Experiment (CASIE) in 2009. Findings from geostatistical analysis of the CASIE data are reported and related to sea-ice modeling in [31].

(2) GPS data. Two separate GPS units were used for redundancy. The first, called "Button GPS", is a low cost, plug-and-play type used for making quick, low-accuracy plots and serves as a backup for the second system. Button GPS was placed on the dashboard of the helicopter, where it had good sky view through the large front window. The second system is a high-cost high-accuracy two-part GPS system, which consists of a base station reference receiver and a helicopter mounted kinematic GPS unit (rover). The base station collects observations including atmospheric delay parameters and orbit information that allow for post-processing that increases the position accuracy of the kinematic GPS unit mounted on the helicopter. Sky view of the base station was unobstructed, because the base station was positioned on an elevated moraine edge or near a cliff edge on the southern side of Negribreen, several hundred meters above the glacier (Figure 3a,b). There were no large mountains obstructing the sky view of the base station. The rover was mounted on one of the skids of the helicopter, and thus the body of the helicopter and the helicopter rotors possibly interfered with sky view of the rover. The instrumentation for the differential GPS data collection was provided by UNAVCO in both years.

(3) IMU data. IMU data record the attitude of the helicopter during the flights. These data are collected to allow correction for attitude and vibration. The IMU is also owned by our Geomathematics Laboratory and integrated into the survey system. Our post-processing includes coincidently collected IMU data to remove helicopter vibration with a low-pass filter, and to correct for roll, pitch, and yaw with a transformation matrix, taking into account the spatial offset between the mounting positions of the laser altimeter system and the GPS rover on the helicopter.

Table 3. Technical specifications of the Universal Laser System (ULS) and settings during the Negribreen airborne geophysical observation and validation campaigns in 2017, 2018 and 2019. FDA—United States of America, Federal Food and Drug Administration, CFR—Code of Federal Regulations Title 21, see https://www.accessdata.fda.gov/scripts/cdrh/cfdocs/cfcfr/cfrsearch.cfm?FR=1040.10 (accessed on 3 October 2021).

Manufacturer	Laser Technology, Inc.
Model	Universal Laser System (ULS)
Wavelength	905 nm (IR)
Beam Divergence	3 mrad (∼30 cm diameter footprint at 100 m range)
Exit Aperture	42 mm
Pulse Repetition Frequency (PRF)	10–4500 Hz, configurable, 4000 Hz for Negribreen campaign
Averaging	10 points for Negribreen campaign (400 Hz effective PRF)
Maximum Range Over Ice Targets	500 m
Eye Safety	Class 1, 7mm eye safe (FDA,CFR21)
Accuracy	±2 cm
Resolution	1 mm
Dimensions	5.3 in L × 4.75 in W × 2.5 in H
Weight	1.75 lbs (0.8 kg)

(4) GoPro time-lapse-imagery was recorded at two images per second in linear imaging mode. The linear mode was selected, because it yields the least distortion of the imagery. Time-lapse imagery is better suited for comparison with discrete altimeter data than video data, results in much smaller data volumes and reduces battery energy usage.

(5) Photographs were taken using handheld cameras to provide overviews of the glacier system during surge, especially from high altitudes above ground level (a.g.l.), to collect documentation of crevasse provinces, calving events and other features of special interest to the study of the surge process. Several thousand images were taken during each flight.

4. Comparison of Different Approaches to GPS-Data Collection and Processing: Real-Time Kinematic (RTK) Compared to Kinematic GPS Data Collection with Differential Correction Using Base and Rover Data

4.1. Scientific Motivation and Experiments

In preparation of the ICESat-2 launch (15 September 2018), in summer 2018 we carried out experiments aimed at optimizing GPS data collection and resultant repeat accuracy of satellite ground tracks during airborne validation flights of ICESat-2 measurement capabilities. These include experiments with Real-Time Kinematic (RTK) data collection, which are motivated as described in the following paragraphs.

There is relatively little knowledge of the geodetical accuracy that can be obtained from kinematic data collection from a fast-moving platform, especially from a helicopter that is susceptible to wind and turbulence. In an approach that utilizes a base and rover with post-processed solutions, the challenge is to acquire sufficient satellite views to maintain a fixed solution in the GPS post-processing for at least 10 min, while the helicopter is flying. The faster the vehicle/rover moves, and the less linearly due to turbulence, the harder it is to find solutions. The mounting location of the GPS receiver and, for a helicopter, interference with rotor blade occultation, create additional unknowns [32].

The problem is compounded by the limited mounting options for a GPS rover on a helicopter. In our Svalbard experiments, the rover had to be mounted on one of the skids for safety reasons, where it had limited sky view due to the body of the helicopter and the rotors. Therefore, we included experiments of RTK data collection in our 2018 experiments, as an alternative to the post-processed base-rover GPS data analysis.

Combining the 2018 pre-launch experiments with 2019 experiments along near-time ICESat-2 tracks, we have results from three types of GPS experiments:

(1) Kinematic GPS data collection with differential correction using base and rover data (summer 2018)
(2) Real-time kinematic (RTK) GPS data collection using base and rover data (summer 2018)
(3) Kinematic GPS data collection with differential correction of rover data using Natural Resources Canada Spatial Reference System Precise Point Positioning (CSRS-PPP, [33,34]), (summer 2019)

Type 1 GPS experiments involve setting up a GPS base station at the side of the glacier on an elevated moraine or near a cliff edge for the duration of the airborne survey, typically two hours over the Negribreen region, and collecting kinematic data with a rover GPS mounted to the helicopter. During these experiments, the pilot follows a predetermined flight path. Experiments of best flight path segmentation were carried out. After the field experiment, base station data, recorded at 10Hz, are used to differentially correct rover data, also collected at 10 Hz. Because of regulations of the governor of Svalbard, the GPS base cannot be left in the glacier region. While a 24 h recording time for the base would be preferred, the length of time of about 2 h has been found to be sufficient for the accuracy of the project objectives.

Type 2 experiments require a base station and a rover as well. But in contrast to type-1 experiments, during RTK data collection, the correction of the rover position is carried out during the flight, using information sent over by the base station, and displayed on a blue-tooth-enabled device. This enables a correction of the flight path during flight.

In 2019, the GPS base station malfunctioned or was set incorrectly, recording only 15-second data, thus the differential correction applied to the 2019 GPS rover data uses Spatial Reference System Precise Point Positioning (CSRS-PPP), a service provided by Canadian Geodetic Survey, Natural Resources Canada, for post processing [33,34]. This situation yields an unintentional third type of experiment, whose results may be of interest for flights where a base station cannot be placed.

4.2. Results

(1) Kinematic GPS data collection with differential correction of rover data with base station data in post-processing yields the highest accuracy of positioning, of our three types of experiments. Experiments on flight-path segmentation indicate that quarter-crossings of the glacier work best, aiming to fly a straight line across a 2–3 km distance. Full glacier crossings are similarly good with respect to resultant accuracy of track repeats and require fewer waypoints to be entered manually by the pilot into his on-board system. Notably, the entire survey setup requires good collaboration and communication between the pilot, the experiment lead (the PI) and the survey team who continuously monitors instrument functionality and height (altimeter range). As a result, full glacier crossings of about 10–20 km flight distance depending on location were used in 2019.

(2) Experiments with RTK indicated that the added accuracy from the real-time-kinematic correction is more than offset by the inaccuracies introduced by the continued reactions of the pilot to adjust the flightpath and thus the aircraft attitude to the updated position information (from the RTK system). Flying straight towards points, predetermined by the expedition lead/ scientist with 2–4 points for a glacier crossing of 10–20 km track length and shared with the pilot prior to the flight, yields data from a more "quiet" helicopter flight and more consistent, linearly interpolatable data. Thus, the repeat accuracy of a pre-determined satellite track is not limited by the accuracy of the GPS solution, but instead by the maneuvering characteristics of a helicopter. The pilot cannot fly a straight path when the quick changes in the RTK-GPS directions call for unpractically frequent changes of the flight direction of the helicopter. A helicopter turn necessitates leaning the helicopter to the side, which then introduces additional distortions to the flight path and results in off-nadir laser pointing.

(3) Results from CSRS-PPP [33,34] are sufficiently accurate for validation of ICESat-2 surface height determination and morphological characteristics, as will be detailed in the following sections, while most likely significantly less accurate than positions differentially corrected with a base station. The CSRS post-processing uses precise satellite orbits, clock and bias corrections from a global network of receivers. Because of the much shorter base line resultant from a placing a base station in the field area, differential corrections using a locally placed base station are known to yield highest accuracy [35].

(4) Despite the problem of interference of the rotor blades and the helicopter body with view of GPS satellites, the amount of GPS rover data collected was found to be sufficient for accurate geolocation of the ULS data, despite the mounting location of the GPS rover on the skids.

(5) Outlook: Based on the 2018 and 2019 experiments (and previous experiments in similar types of field surveys), highest accuracy will be achieved by using differential GPS with a base station on the side of the glacier (as shorter baselines yield higher position accuracy) and a GPS rover on the aircraft. It may be easiest, especially for students new to GPS data collection, to utilize a rover and a base GPS instrument from the same brand, while not necessary to process the data (which can be converted to RINEX format independently of the receiver brand). Trimble has a proprietary format, but RINEX conversion remains a possibility.

The summer 2018 data are not used in the remainder of this paper, because they were collected prior to the launch of ICESat-2 on 15 September 2018.

5. Surface-Height Determination from Synchronization of Laser and GPS and IMU Corrections

5.1. Processing of 2019 GPS Data

Processing of 2019 GPS data was carried out using the following steps:

(1) GPS data were downloaded from the rover and the base station. In the 2019, flight 2 GPS recordings, the base station recorded only 15s-data. The rover recorded at 10Hz. In the differential data analysis, using the rover/base data, we were not able to obtain a fixed solution in the Trimble Business Center (TBC), only a float solution. We attribute this to the likely possibility that the rover was not tracking a sufficient number of satellite vehicles (SVs) to get a fixed solution. Therefore, the following steps were undertaken to obtain a solution.

(2) GPS data from the rover (Trimble R10) *(rover_data_set_v1.T02)* were converted from Trimble format (.T02) to RINEX (Receiver INdependent EXchange format) *(rover_data_set_v2.RINEX)*. This is performed using Trimble's Convert to RINEX utility (accessed on 3 October 2021).

(3) The RINEX *(rover_data_set_v2.RINEX)* file is submitted to the Spatial Reference System Precise Point Positioning (CSRS-PPP), provided by Natural Resources of Canada. CSRS-PPP is an online application for global navigation satellite systems (GNSS) data post-processing. It uses precise satellite orbit, clock and bias corrections derived from a global network of receivers to determine accurate user positions anywhere on the globe, regardless of proximity to reference stations (from: https://www.nrcan.gc.ca/maps-tools-and-publications/tools/geodetic-reference-systems/data/10923 (accessed on 3 October 2021)). Upon submission of RINEX files, enhanced positioning precisions in the North American Datum of 1983 of the Canadian Spatial Reference System (NAD83(CSRS)) or the International Terrestrial Reference System (ITRS) in realization ITRF14 are returned.

In essence, the CSRS software was able to provide a fixed solution for the rover data. To best match with the ICESat-2 data and their coordinate reference, we selected ITRF14 as the reference frame for the CSRS-PPP solutions. The coordinates used in this analysis are given as *(rover_data_set_PPP_v3)*, in csv format (human readable, including lat, lon, elevation, time, reference frame) with reference to ITRF14. The Canadian Geodetic Survey uses the GRS80 ellipsoid (a_e = 6,378,137 m, $\frac{1}{f} = 298.257222101$) for the realization of ITRF14 in CSRS-PPP (Brian Donahue, Canadian Geodetic Survey, friendly pers. comm. 19 January

2022). For practical purposes, the ITRF14 corresponds to WGS84 (conversion from ITRF14 to WGS84 results in identical coordinates, for a more precise description, see Section 2). In summary, practically the same coordinate reference is utilized for the airborne data and the ICESat-2 ATLAS data.

5.2. Comparison of Button GPS and Corrected Rover GPS Data

In addition to the rover GPS, GPS data were also collected using a simple instrument, the Button GPS, located on board the helicopter. The Button GPS is a plug-and-play type inexpensive instrument, that is placed under the windshield of the helicopter and has proven to be very reliable during several years of airborne campaigns. The Button GPS records location at 1 Hz, while the rover GPS records location at 10 Hz. This Button GPS has lower accuracy, especially of height data, and lower frequency than the rover GPS, but is directly connected to the ULS laser system and records on the same computer. The rover GPS recorded only time-from-start-of-rover-time, it records on a GPS-internal computer and hence its times are independent of the ULS. Thus, we are using the time stamps from the Button GPS to align the corrected rover-GPS data with the ULS measurements.

This process is illustrated in Figure 5, which shows heights and times from the two GPS receivers during flight 2. Button GPS recordings appear to be "ahead of" the rover GPS with respect to distance, an effect that results from starting the Button GPS first. Since the Button GPS and ULS laser were being controlled from the same computer, we have exact time synchronization between them. In contrast, the rover GPS was controlled through its internal computer (and a handheld controller), which results in timing independent from that of the ULS laser. The first correction step involved time-shifting the rover GPS to align with the Button GPS/ULS laser (Figure 5).

5.3. Derivation of Surface Height Using ULS and Differential GPS or Button GPS

Ice-surface height is calculated by subtracting the laser-retrieved height from the GPS-retrieved height. Two apparent surface height values result from pairing ULS data with rover GPS data and Button GPS data (Figure 3b). In addition to the time lags between the rover GPS and the ULS laser, the change in height of the aircraft and the surface roughness of the glacier contribute to the apparent differences in height. For example, when the GPS starts to move down (aircraft lowers), the laser-retrieved height would normally be lower as well. However, in our case, the laser is ahead of the GPS, so it has already started recording lower heights. The different start times contribute a small part of the large apparent height difference values between the rover GPS-ULS and the Button GPS-ULS data, the main source of the apparent height difference is the poor height determination of the Button GPS. ULS data with ranges greater than 500 m are excluded from the analysis, as the ULS does not provide enough returns at ranges larger than 500 m (see Section 7).

5.4. Synchronization of Laser and Differential GPS and Button GPS

Crevasse locations are used to further improve the determination of a time shift, performed visually to match. Time accuracy is 0.1 s. Results in Figure 5c show that crevasse morphology lines up in the recordings of the Button GPS and the differential GPS, thus using crevasse morphology to aid in determination of a time shift is a feasible approach. There are still height differences on the order of tens of meters, which are due to the inherent properties of the low-resolution Button GPS. Because absolute heights from Button GPS data are less accurate than heights from corrected rover GPS data, heights from corrected rover GPS data are used in the following analysis.

5.5. IMU Correction

An Inertial Measurement Unit (IMU) records the attitude of the survey platform, here the helicopter, during flight, at (in our case) a frequency of 1 Hz. As the laser operates from the helicopter, it actually measures the range from the helicopter to the Earth's surface, rather than the height above the surface, and along a vector to the ground that

is not normal to the ground surface. The IMU correction is a change of reference system, from that centered at the moving helicopter to an Earth-centric system. Prior to the actual correction, a low pass filter (moving average filter) is applied to remove helicopter vibration from the IMU data. The attitude reported by the IMU sensor is utilized in the form of Euler angles for correcting lidar laser range returns, and an orientation matrix for correcting the location of the range measurement in (x,y) coordinates. Formally, the IMU correction utilizes a quaternion multiplication (introduced e.g., in [36]). The IMU correction is applied to the GPS-corrected ULS data (with GPS corrections as described in Sections 5.1–5.4). It should be noted that the IMU corrections do not only yield corrected locations on the ground, but also corrections of the range values (this is a matrix multiplication applied to all components of the ULS data).

Figure 6a,b shows the magnitudes of the components (roll, pitch and yaw) of the IMU corrections. Figure 6c,d illustrates the magnitude of range corrections. At the scale of absolute range, this is not resolved (in Figure 6c,d). The correction magnitude (Figure 6c,d) is less than 5 m on average, with some spikes up to 10 m. These usually occur when the aircraft is turning or during heavy winds. We experienced heavy winds near the end of flight 2, which explains the largest difference.

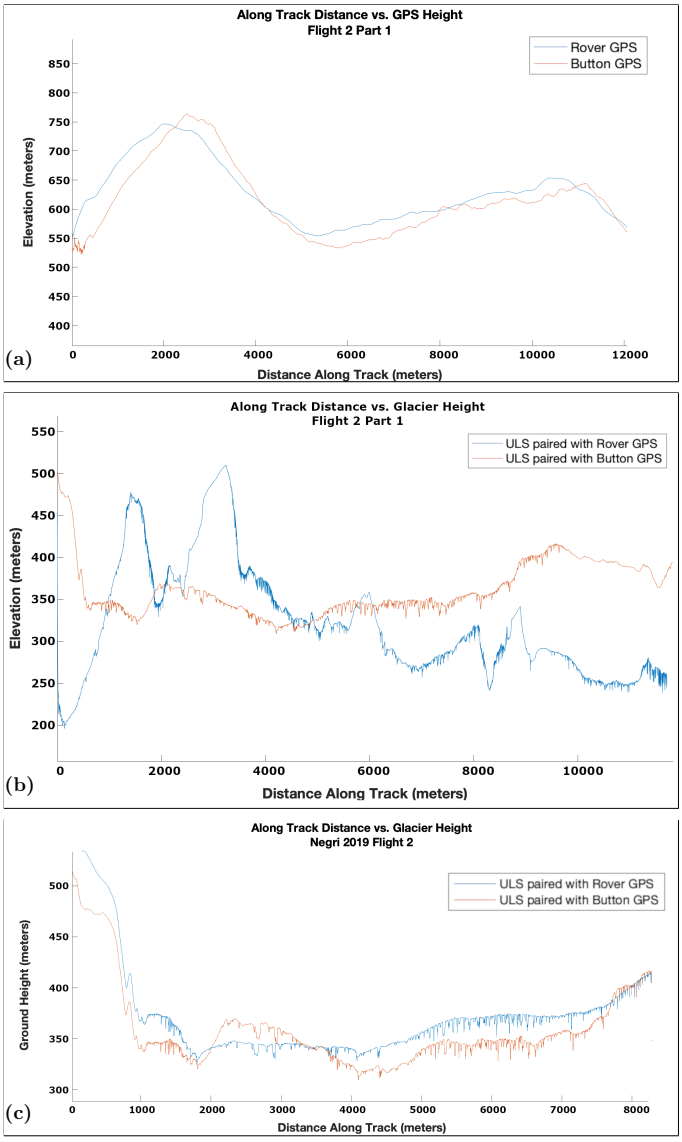

Figure 5. Illustration of the process of surface-height determination from synchronization of ULS and GPS data. Negribreen validation campaign. Flight 2, 13 August 2019. Corrected GPS data are used

(see Equation (1)). (**a**) Comparison of GPS heights and times from two GPS receivers. Button GPS (red), recorded at 1 Hz, started first, together with ULS and recorded on the same computer as the ULS (exact time synchronization of ULS and Button GPS). Rover GPS (blue), recorded at 10 Hz, started second, time recorded on the GPS-internal computer. The first correction step is time-shifting the rover GPS to align with the Button GPS/ULS laser. (**b**) ULS apparent surface heights, derived when pairing ULS data with Rover GPS data (blue) and Button GPS data (red). (**c**) ULS surface heights, after time-shift correction between ULS laser and the rover GPS. Now both elevation measurements and crevasse morphologies resemble each other.

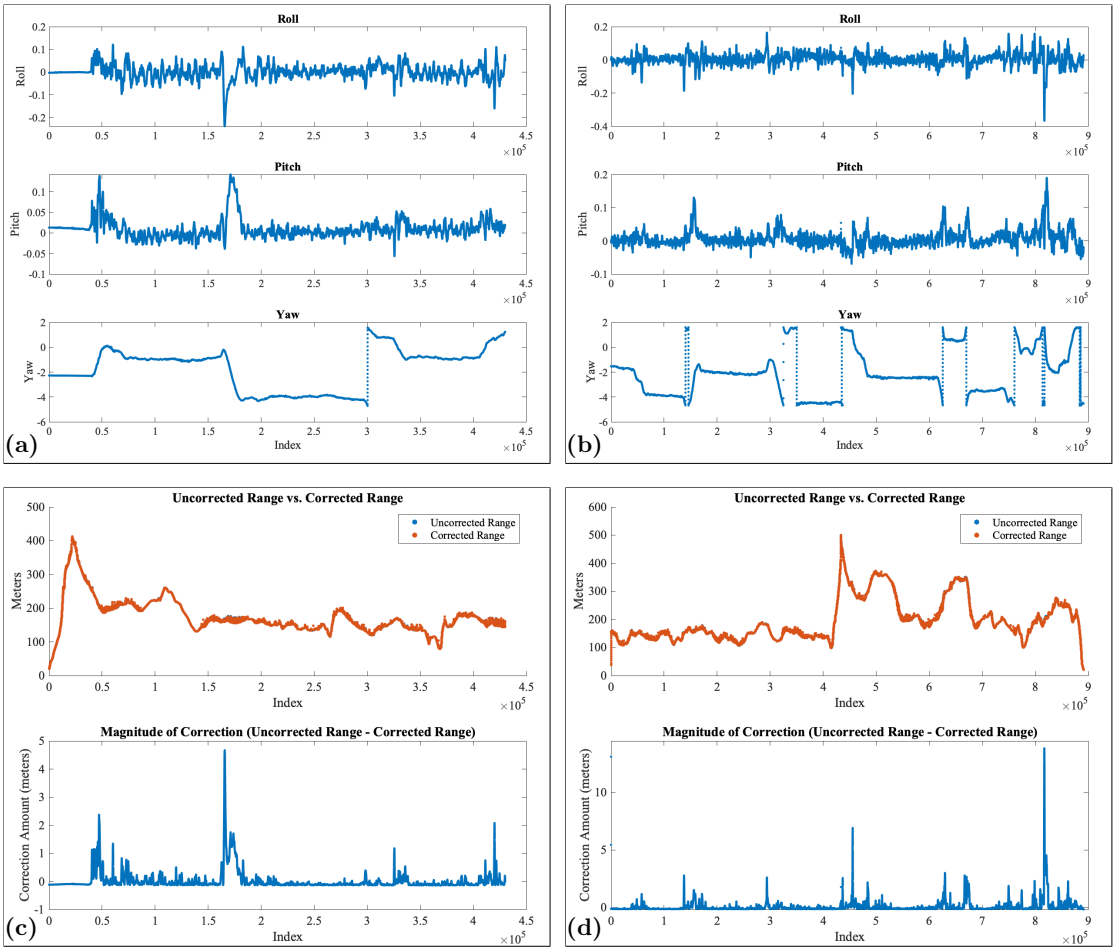

Figure 6. IMU values and IMU-corrected ULS ranges. Negribreen validation campaign. Flight 2, 13 August 2019. (**a**,**b**) IMU values (roll, pitch and yaw) for flight2, part1 (**a**) and flight2, part2 (**b**). (**c**,**d**) Range correction (total corrected and uncorrected range and magnitude of correction) for flight2, part1 (**c**) and flight2, part2 (**d**).

6. Analysis of Airborne Geophysical Data and Results: Ice-Surface Heights, Technical Information and Crossover Analysis

In this section, we analyze the airborne geophysical data (without comparison to ICESat-2 data) to derive ULS range and ULS-based ice surface heights along flight tracks (Section 6.1). Section 6.2 is devoted to technical information that may be useful to design future airborne validation campaigns from small aircraft, including helicopter velocity, optimal ULS range and aircraft altitude above ground, resultant data frequency and on-ice spacing. These results generalize to other types of manned aircraft and to some extent, unmanned aircraft. Precision of the ULS height data in crevassed terrain is assessed using a crossover analysis (Section 6.3).

6.1. Results Part 1: ULS Range and Ice-Surface Heights Based on GPS and IMU-Corrected Data

Following the GPS and IMU corrections as described in Section 5, we now have the correctly geolocated coordinates for the ULS data. After application of the IMU and GPS geodetical corrections to the ULS data, we obtain ULS data with geographical coordinates

$$x_{geogcorr} = (lat_{corr}, lon_{corr}, z_{corr}), \quad (1)$$

where z_{corr} is the corrected surface height. As described above, the GPS coordinates are given in IRTF14 (as output from the CSRS-PPP software). The bounce point of the ATLAS signal is also given in the IRTF14 reference frame as latitude, longitude and height w.r.t. the WGS-84 (G1150) ellipsoid for each point in the photon cloud reported on the ATL03 data product [2,3,18,22] (Section 2.1). Therefore, corrected ULS data from the validation campaign are directly comparable to ATL03 data.

Lastly, ULS data $x_{geogcorr}$ given with reference to the geographic coordinate system are converted to ULS data with reference to the Universal Transverse Mercator (UTM) coordinate system

$$x_{utmcorr} = (north_{corr}, east_{corr}, up_{corr}) \quad (2)$$

with reference to the WGS84 ellipsoid and UTM zone 33 (central meridian 15° E). We use $up_{corr} = z_{corr}$. We are now able to determine the range of the ULS to the ice surface at the laser measurement rate (Figure 7a), which combined with the aircraft position gives the surface height of the glacier (Figure 7b). The corrected surface heights can be used in several glaciological applications, including monitoring of surface elevation change during the surge, indicative of mass transfer during the surge, and derivation of the spatial characteristics of the crevassed ice surface (see, Section 7).

6.2. Results Part 2: Technical Information: Helicopter Velocity, ULS Range, Data Frequency and On-Ice-Spacing

The range of the ULS is an important experiment parameter to control, as the ULS functions for altitudes up to about 500 m and works best for shorter ranges up to about 300 m. Helicopter safety requires that the instrument be flown at sufficient distance above the surface, dependent on (a) visibility and surface reflectance, and (b) topographic relief, morphology and crevassity of the terrain. Following [11], we use the term "crevassity" as a measure of the void fraction in glacier ice as a material, akin to porosity. Crevassity is utilized here as a general term to describe the magnitude and complexity of the overall deformation at a given location, which for a surge glacier manifests itself in the crevasse characteristics.

All ICESat-2 validation flight lines were flown at this optimal height range, with tracks in the upper central Negribreen (inlcuding those for RGT 450 and RGT 594) collected with a range of 100-200 m and tracks traversing towards the upper inflows flown at 200–350 m range (Figure 7a). The ULS is originally designed for measurements at much shorter ranges and there is no practical lower limit of the measurement range (we test the instrument in the laboratory, for distances down to 1 m). The practical lower limit of the range is constrained by flight operations safety, as the helicopter pilot needs to maintain a safe height above the highly reflective, sloping and crevassed ice surface, at a flight speed that is efficient for data collection.

Flight velocity magnitudes, evaluated after GPS and IMU corrections, are given in Figure 7c and after along-track smoothing in Figure 7d. Speeds for the validation tracks (RGT 450 and RGT 594) are generally between 25 m/s (90 km/h) and 35 m/s (126 km/h), slower over steep ice falls. Averaged helicopter velocities were 17 m/s (averaged for the whole survey flight) and 30–35 m/s while flying over the ICESat-2 segments. Mean velocities were 34.426 m/s over the RGT 450 segment and 32.0451 m/s over the RGT 594 segment. The ULS functions well at higher velocities as well, as supported by the fact that frequency of recorded data is generally close to the 400 Hz nominal frequency of ULS

setting used during our experiments (Figure 7e, for ULS settings, see Table 3). Resultant on-ice along-track spacing was 0.06–0.08 m for the validation tracks (Figure 7f).

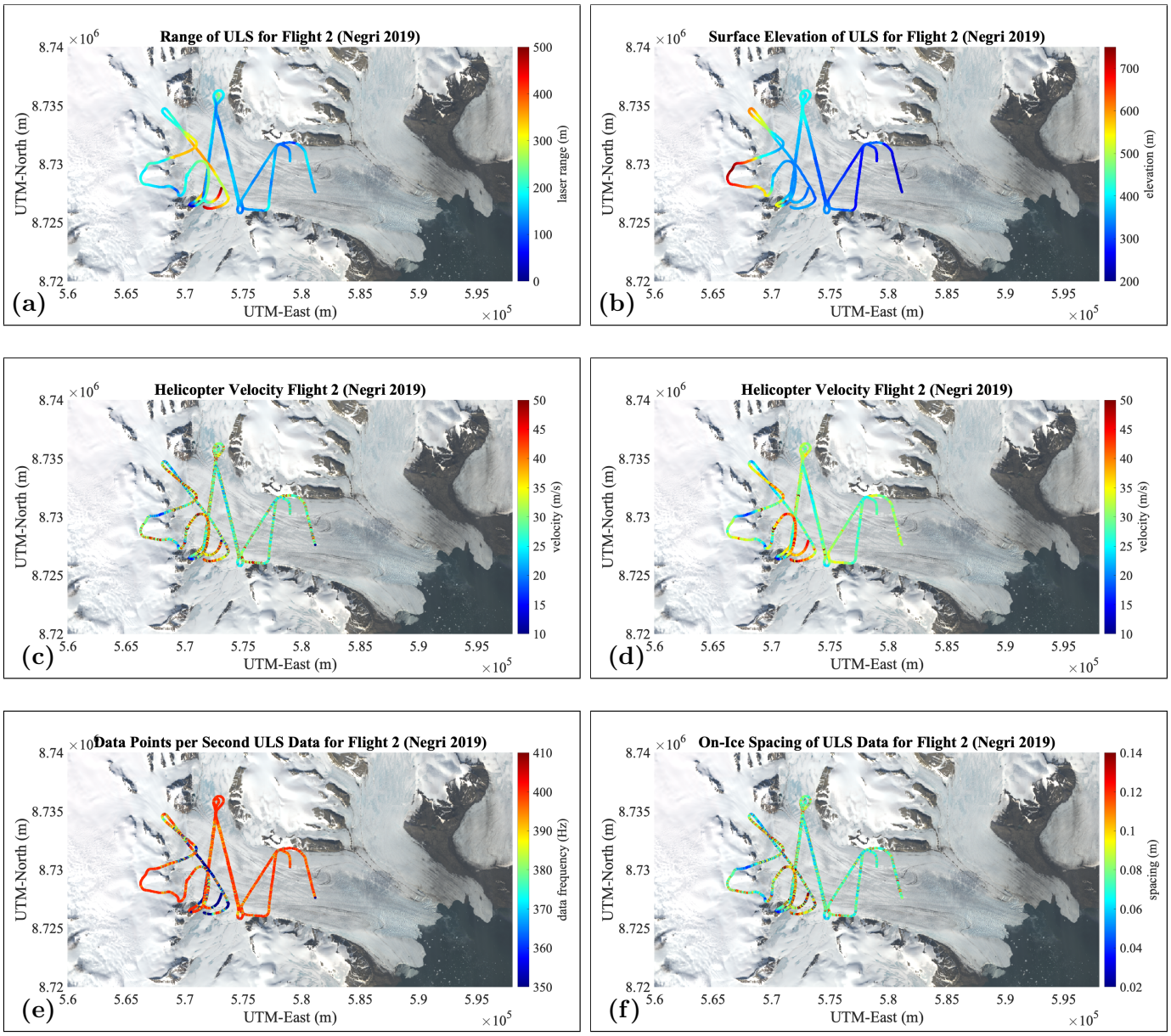

Figure 7. Results from ULS data collection. Negribreen validation campaign. Flight 2, 13 August 2019. The scale does not allow for identification of crevassed regions. (**a**) ULS range aircraft to ice surface. (**b**) ULS surface height (elevation). (**c**) Aircraft velocity magnitude. (**d**) Aircraft velocity magnitude, smoothed. (**e**) Data points per second. (**f**) On-ice spacing of ULS data. Background: Landsat-8 image from 5 August 2019 [LC08_L1TP_215003_20190805_20190820_01_T1].

Flight altitudes above ground are further constrained by the other instruments: Higher altitudes allow collection of better imagery, i.e., imagery that shows larger crevassed regions. Flight altitudes of 10 km or more are flown for collection of overview imagery. Altitude in transit from one observation target to another can be higher than 300 m and still yield altimeter data useful for science. For example, the blue stretch in Figure 7e is flown at 400 m above ground, resulting in lower data frequency and somewhat larger on-ice spacing of 0.08–0.14 m. ULS data with ranges greater than 500 m are excluded from the analysis, as the ULS does not work properly at this range, and the situation of large ranges only occurs when we flew high to collect overview imagery and the ULS was not turned

off. In conclusion, the ULS can be operated with full recording frequency for altitudes up to 300 m above ground level (a.g.l.). The advantage of flying at lower altitudes a.g.l. is that the on-ground spacing is smaller, as the spacing is a direct function of altitude above ground. Between 300 m and 500 m, the recording frequency can drop somewhat, but still yield useful science data. Lower altitudes of 100 m can be used for flights with unmanned aerial systems over sea ice, where risk is lower and the surface is flat, as during the Characterization of Arctic Sea Ice Experiment (CASIE) [30,31].

6.3. Results Part 3: Crossover Analysis of ULS Heights

The crossover analysis is performed on the corrected height estimates for the 2019 flight data in the upper glacier (see Table 4). Crossover height differences are calculated after averaging all points within a 10 m radius of the intersection location for each crossing flight segment, resultant in 14 crossover locations with a mean elevation difference of 0.111 ± 3.056 m. Similar values are achieved when the averaging radius is 1 m and 0.1 m. Largest differences (red and dark blue points in Figure 8) occur at locations where the aircraft is turning significantly, where laser ranges are large and IMU corrections are most relied upon, and at locations of large crevasses where height variations on the order of tens of meters occur. However, most of the crossover differences are near zero (green points) when the aircraft is flying straight over non-crevassed areas or areas with beginning crevassing. If we remove the 3 crossover locations that occur on significant turns, we obtain a mean elevation difference of -0.172 ± 2.564 m for the remaining 11 points. Since underflights of ICESat-2 tracks follow straight flight paths, the estimated the precision of our measurements is approximately 2.6 m in crevassed terrain. Accuracy estimates would require ground elevation truths independent of and coincident with our flight data, however collection of ground measurements on a glacier during surge is not feasible (dangerous). Crevasse depths ranging to 45 m were observed with ICESat-2 and determined with the DDA-ice [3].

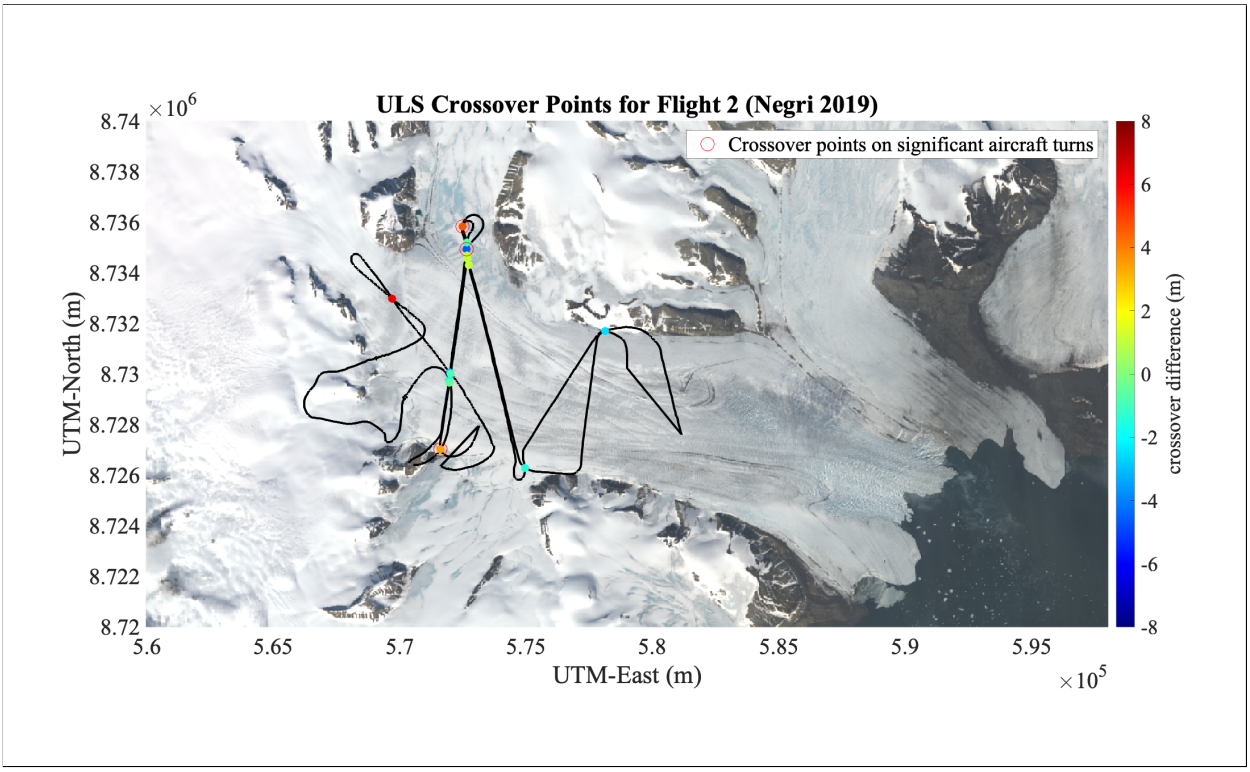

Figure 8. Crossover elevations from ULS data collection. Negribreen validation campaign. Flight 2, 13 August 2019. There are 14 crossover locations. Removing the three crossover points on large turns, for the remaining 11 points the mean difference is -0.172 ± 2.564 m. Background: Landsat-8 image from 5 August 2019 [LC08_L1TP_215003_20190805_20190820_01_T1].

Table 4. Crossover analysis for Flight 2, 13 August 2019, Negribreen ICESat-2 Validation Campaign 2019. Estimates are given when using all crossover locations (seen in Figure 8) and for locations only along relatively straight flight segments, i.e., where the helicopter was not performing a significant turning maneuver. Crossover estimates are averaged within a radius specified in the last column of the table.

	Mean Elevation Difference (m)	Standard Deviation of Elevation Difference (m)	Number of Points	Crossover Radius (m)
All Crossover Locations	0.111	3.056	14	10
Crossover Locations Excluding Turns	−0.172	2.564	11	10

7. Analysis of Geolocated ULS and ICESat-2 ATLAS Data

7.1. Overview

Following the geodetical and technical results in the last sections, we now have established the technical basis needed to (1) quantitatively investigate the capability of a light-weight experiment using a small helicopter to repeat satellite tracks accurately and (2) compare surface heights and crevasse morphologies from ULS and ATLAS measurements. Results relating to the first topic will be summarized in Section 8 and results regarding the second topic will be reported in Section 9. Here, the analysis is carried out as a case study for each of five sets of tracks, to facilitate understanding the relationships between flight-repeat capability of our experiment setup dependent on a number of factors including wind, resultant track separation, crevasse representation in ULS data and in ATLAS data for weak and strong beams, crevasse morphology, crevasse characteristics and surface roughness.

ICESat-2 tracks for RGT 450 and RGT 594 were repeated, including both strong and weak beams, resultant tracks for ULS and ATLAS are shown in Figure 9a,b and listed in Table 5. A useful tool in this context is plotting the results in 1-km along-track segments, as shown in Figure 9. Figure 9a,b provides the 1-km segments for flight 2, parts 1 and 2, respectively, carried out on 13 August 2019 over Negribreen.

Data from flight 1 are not used in the analysis in this paper, because the GPS rover did not record data. Data from the Button GPS are still useful for analysis of surge evolution, reported elsewhere.

Flight 2 has two parts, each part includes an overpass of RGT 594 (gt1 l and gt1r) and RGT 450 (gt1l and gt1r) tracks. The track of the RGT 594 weak beam (gt1r) was overflown twice (both passes in part 2 of flight 2) in order to obtain information on the quantitative measures listed above from a repeat experiment. However, because the weather worsened significantly during flight 2, the first repeat occurred during approximately normal weather conditions and the second one during unusually strong winds of over 30 knots (60 km/h). The increasing winds led the pilot to end the data collection for this day soon after. The three tracks for RGT 594 were flown in the order (1) "RGT 594, gt1r, part 1", (2) "RGT 594, gt1l", (3) "RGT 594, gt1r, part 2", with other flight lines in between, hence wind speed increases in this order. Labels in the figures are as follows: "RGT 594, gt1r, part 1" refers to overpass 1 (less wind). "RGT594, gt1r, part 2" refers to overpass 2 (stronger wind). During strong winds, the pilot has to hold the helicopter at an angle relative to the direction of flight and tilted, which makes following the prescribed tracks a lot harder and increases the IMU values. The IMU still functions for this situation (see Figure 6). Resultant track separations for RGT 594, gt1r, part 2 are higher than for the other tracks, but crevasse comparisons are still useable for evaluation of ICESat-2 tracks, as the analysis will show.

The tracks of the RGT 594 gt1r and gt1l are the location of analysis of 2018 prelaunch Negribreen airborne campaign data and first post-launch ICESat-2 data from early winter 2018 reported elsewhere, which indicated that ICESat-2 measures summer's crevasses

through winter's snow cover. Because the identification of crevasses under snow was based on non-synoptic airborne and satellite data with several months separation, an additional objective for the 2019 validation campaign was the collection of synoptic satellite and airborne data for the same crevasse field surveyed in summer 2018 with the ULS and in winter 2018 with ICESat-2 ATLAS.

In the following subsections, we analyze each of the tracks (1) RGT 450, gt1l (strong beam) (Figure 10), (2) RGT 450, gt1r (weak beam) (Figure 11), (3) RGT 594, gt1l (strong beam) (Figure 12), (4) RGT 594, gt1r (weak beam), overpass 1 (Figure 13), and (5) RGT 594, gt1r (weak beam), overpass 2 (Figure 14).

For each example, we show the location of the ground track sections, indicated by red and green tracks, superimposed on a Landsat image from 5 August 2019 (collected only 8 days before flight 2), in panel (a) of Figures 10–14. Zooming into the area, with the flight tracks plotted over the aforementioned SkySat image from 18 August 2019, gives and impression of the crevasse provinces under the flight tracks, and visually illustrates the across-track distances between the predicted and actual ATLAS tracks and the actual ULS tracks (panel (b) in Figures 10–14). The distances are then given in a graph that illustrates the variability of the distance between the ULS track and the actual ATLAS track, with the distance between the predicted and actual ATLAS tacks added in for comparison (panel (c) of Figures 10–14). Note that at time of flight, only the predicted ATLAS tracks were available, thus we aimed to underfly the predicted tracks for each beam. Track variability is exaggerated by the over-heightened plot style. Variability of the ATLAS-predicted to ATLAS-actual distance is shown in better resolution in panel (d) of Figures 10–14. In summary, capability for track repeat ranges from an average of 11.32 m to 24.87 m, with an outlier of 60m during strong storm conditions. Differences between ICESat-2 predicted and actual range from 6.51 m to 15.65 m for the average difference of a glacier crossing.

Figure panels (e) and (f) in Figures 10–14 aid in the comparative analysis of the surface heights of crevassed regions. Segment lengths in (a), (c), (d) and (e) are the same within each figure and of approximately 2–3 km length, while segment lengths in (b) and (f) show subsets for better representation of the crevasse morphologies. To further aid the comparison of panels (e) and (f), we have added a blue bar in panels (e) that shows the location and coverage of the DDA-ice results seen in figure panels (f) of the same figure. Surface heights of ICESat-2 ATLAS data are derived by application of the DDA-ice, which was briefly described in Section 2.2.

Table 5. Average distances of ATLAS predicted vs. ATLAS actual and ATLAS actual vs. ULS actual. Values calculated for entire glacier crossings. Note that Figures 9–13 highlight 2–3 km sections for each crossing.

RGT_Beam	ATLAS Predicted vs. ATLAS Actual (m)	ATLAS Actual vs. ULS Actual (m)	Figure
450_gt1l (strong)	9.28	20.40	Figure 10
450_gt1r (weak)	6.51	11.32	Figure 11
594_gt1l (strong)	15.65	60.38	Figure 12
594_gt1r (weak) (part 1)	9.16	24.87	Figure 13
594_gt1r (weak) (part 2)	9.16	24.35	Figure 14

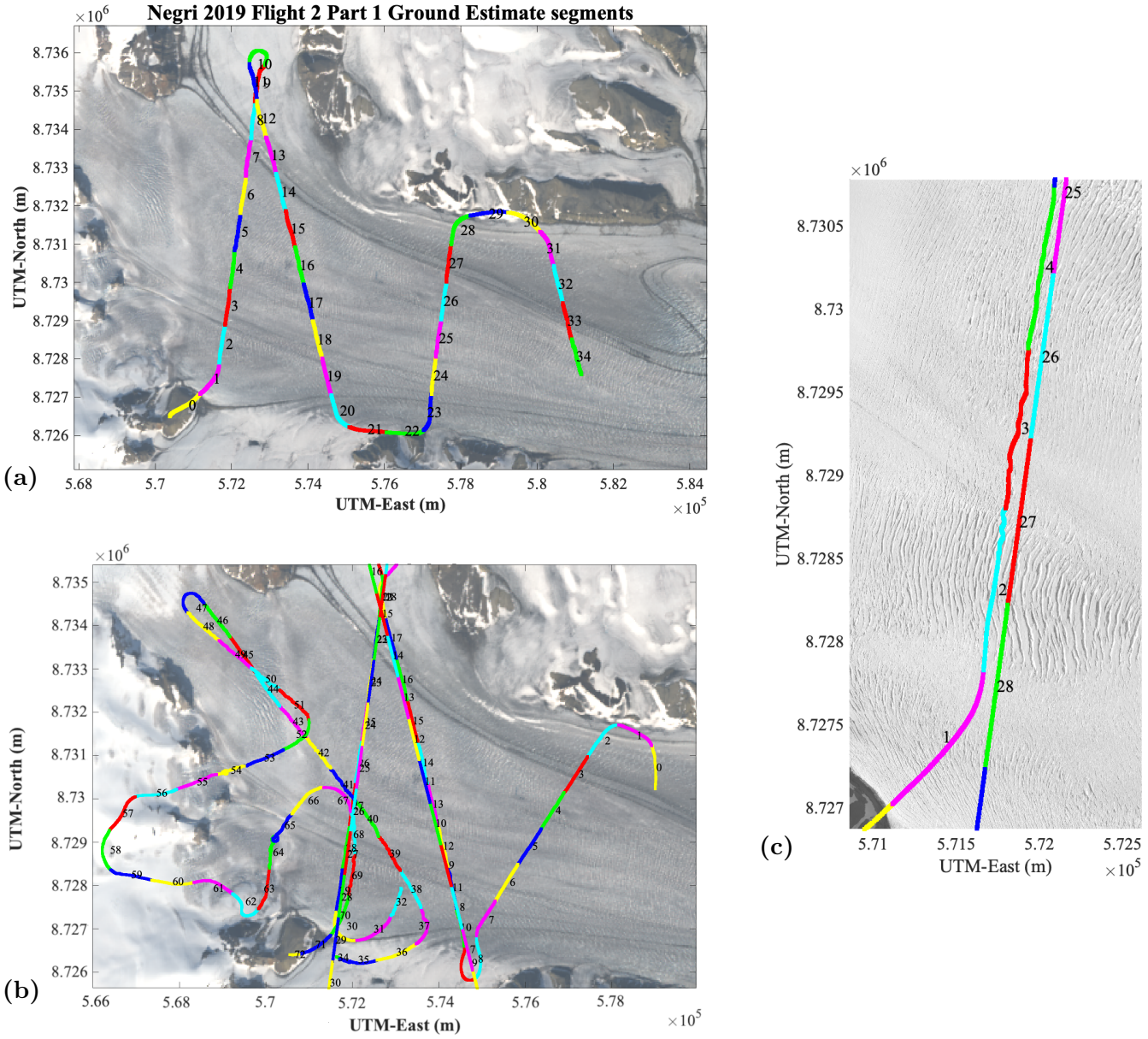

Figure 9. Flight path segments, resultant from ULS data collection, and co-location with ATLAS ground tracks over crevasse fields. Negribreen validation campaign. Flight 2, 13 August 2019. (**a**,**b**) Flight paths, colored in 1-km segments to match the along-track distance vs. elevation plots in Figures 9–13. Background: Landsat-8 image from 5 August 2019 [LC08_L1TP_215003_20190805_20190820_01_T1]. (**a**) Flight 2, part 1. (**b**) Flight 2, part 2. (**c**) Example of co-located airborne ground track (ULS), left, and ATLAS ground track (RG 450 1l), right. Even with an 18 meter average separation, the airborne ground track (ULS) and the ATLAS ground track cross the same crevasse provinces. Background: Planet SkySat image from 18 August 2019 [20190818_150858_ssc9_u0002_panchromatic_dn.tif].

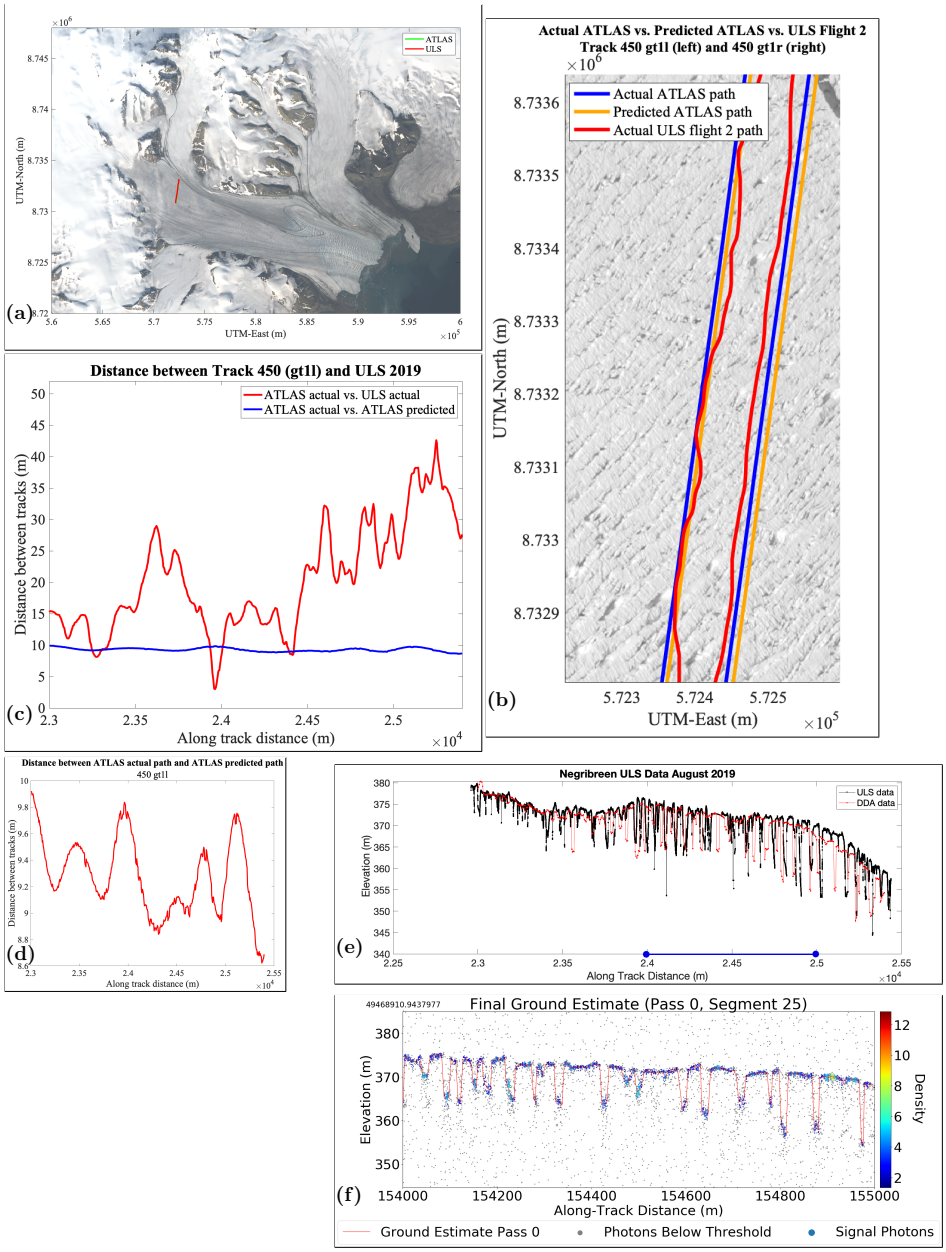

Figure 10. ICESat-2 ATLAS vs. ULS data. Track repeat accuracy and results. RGT 450, gt1l (strong). Negribreen validation campaign. Flight 2, 13 August 2019. (**a**) Location of ATLAS segments over Negribreen and closest ULS data (note the tracks are so close that the green line disappears under the red line). For segment numbering, see Figure 9 (ATLAS DDA segments). Background: Landsat-8 image from 5 August 2019 [LC08_L1TP_215003_20190805_20190820_01_T1]. Segment lengths in (**a**,**c**–**e**) are the same, segments in (**b**,**f**) are subsets. (**b**) Track separation between our ULS flight path, the ATLAS predicted flight path and the ATLAS actual flight path for granule: ATL03_20190727132129_04500405_003_01.h5. Background: Planet SkySat image from 18 August 2019 [20190818_150858_ssc9_u0002_panchromatic_dn.tif]. (**c**) Separations between ATLAS Track 450 (gt1l) actual and ULS flight path, and between ATLAS Track 450 (gt1l) actual and ATLAS Track 450 (gt1l) predicted. Calculated for actual ATLAS and ULS flight paths from data shown in (**b**). (**d**) Track separation between predicted and actual ATLAS 450 (gt1l) flight paths. (**e**) ULS surface heights and ICESat-2 ATLAS DDA-ice surface heights superimposed, after GPS and IMU correction of ULS paths (ground locations). (**f**) ICESat-2 ATLAS surface heights over crevassed region derived using DDA-ice, RGT 450, gt1l, segment 25. DDA-ice parameters as in Table 2. ATL03 data set given in caption for (**c**). Rel. 03 data.

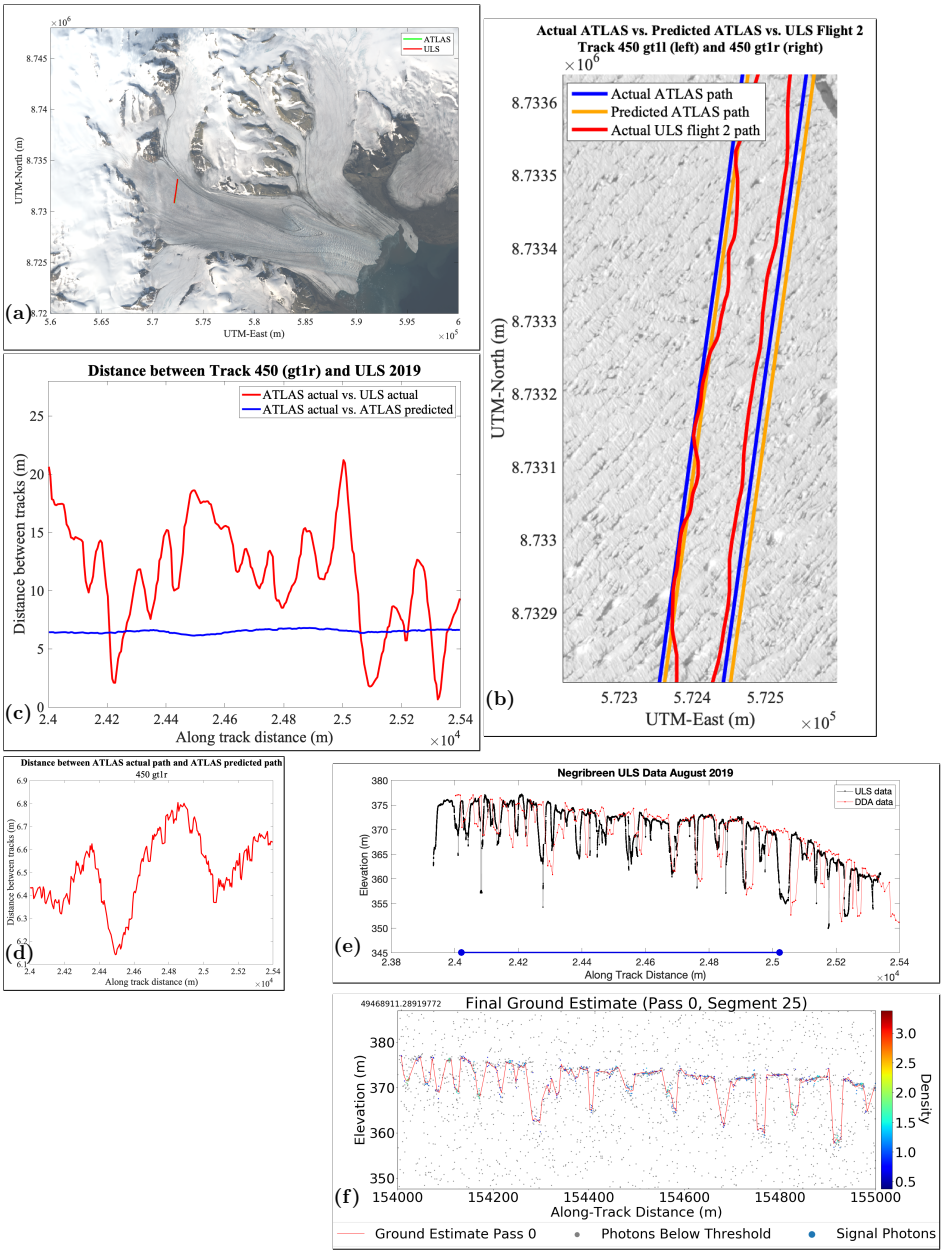

Figure 11. ICESat-2 ATLAS vs. ULS data. Track repeat accuracy and results. RGT 450, gt1r (weak). Negribreen validation campaign. Flight 2, 13 August 2019. (**a**) Location of DDA segments over Negribreen and closest ULS data (note the tracks are so close that the green line disappears under the red line). For segment numbering, see Figure 9 (ATLAS DDA segments). Background: Landsat-8 image from 5 August 2019 [LC08_L1TP_215003_20190805_20190820_01_T1]. Segment lengths in (**a**,**c**–**e**) are the same, segments in (**b**,**f**) are subsets. (**b**) Track separation between our ULS flight path, the ATLAS predicted flight path and the ATLAS actual flight path for granule: ATL03_20190727132129_04500405_003_01.h5. Background: Planet SkySat image from 18 August 2019 [20190818_150858_ssc9_u0002_panchromatic_dn.tif]. (**c**) Separations between ATLAS Track 450 (gt1r) actual and ULS flight path, and between ATLAS Track 450 (gt1r) actual and ATLAS Track 450 (gt1r) predicted. Calculated for actual ATLAS and ULS flight paths from data shown in (**b**). (**d**) Track separation between predicted and actual ATLAS 450 (gt1r) flight paths. (**e**) ULS surface heights and ICESat-2 ATLAS DDA-ice surface heights superimposed, after GPS and IMU correction of ULS paths (ground locations). Blue line: Section covered in f. (**f**) ICESat-2 ATLAS surface heights over crevassed region derived using DDA-ice, RGT 450, gt1l, segment 25. DDA-ice parameters as in Table 2. ATL03 data set given in caption for (**c**). Rel. 03 data.

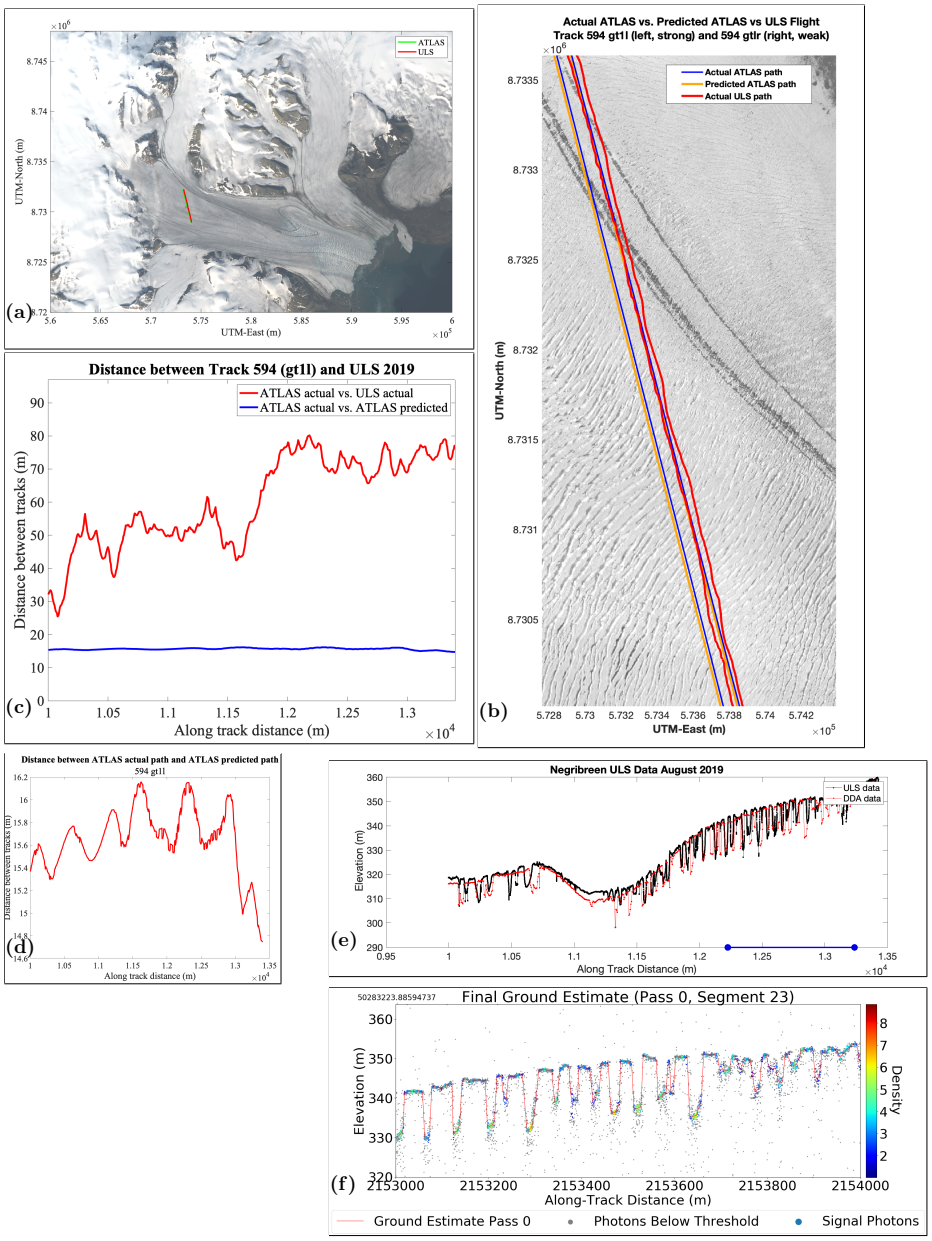

Figure 12. ICESat-2 ATLAS vs. ULS data. Track repeat accuracy and results. RGT 594, gt1l (strong). Negribreen validation campaign. Flight 2, 13 August 2019. (**a**) Location of DDA segments over Negribreen and closest ULS data. For segment numbering, see Figure 9 (ATLAS DDA segments). Background: Landsat-8 image from 5 August 2019 [LC08_L1TP_215003_20190805_20190820_01_T1]. Segment lengths in (**a**,**c**–**e**) are the same, segments in (**b**,**f**) are subsets. (**b**) Track separation between our ULS flight path, the ATLAS predicted flight path, and the ATLAS actual flight path for granule: [ATL03_20190805232841_05940403_002_01.h5]. Background: Planet SkySat image from 18 August 2019 [20190818_150858_ssc9_u0002_panchromatic_dn.tif]. (**c**) Separations between ATLAS Track 594 (gt1l) actual and ULS flight path, and between ATLAS Track 594 (gt1l) actual and ATLAS Track 594 (gt1l) predicted. Calculated for actual ATLAS and ULS flight paths from data shown in (**b**). (**d**) Track separation between predicted and actual ATLAS 594 (gt1l) flight paths; same segment length as in (**a**,**c**). (**e**) ULS surface heights and ICESat-2 ATLAS DDA-ice surface heights superimposed, after GPS and IMU correction of ULS paths (ground locations). Blue line: Section covered in f. (**f**) ICESat-2 ATLAS surface heights over crevassed region derived using DDA-ice, RGT 594, gt1l, segment 23. DDA-ice parameters as in Table 2. ATL03 data set given in caption for (**c**). Rel. 03 data (see, [3]).

7.2. Concepts of Crevasse Provinces and Surface Roughness

Important concepts in the analysis of ice dynamics, especially for glacial accelerations which lead to heavy crevassing as is the case during a surge, are crevasse provinces and ice-surface roughness. The analysis of crevasse provinces allows study of the deformation characteristics of a glacier during surge and provides information on several aspects of ice dynamics, which can be modeled [7,9,11,37]. The mathematically easiest way to distinguish crevassity is through calculation of ice-surface roughness [8,11].

The concepts are illustrated in Figure 9c. A crevasse province is defined as an area that is homogeneous with respect to crevasse type, or ice deformation, and maximal with this homogeneity property [8]. For example, a province of slightly curved, wide surge crevasses extends for almost exactly segment 2 of the flight track and half of segments 27 and 28 of the satellite track. A different province of more narrowly spaced, less open and partly snow-filled crevasses extends northwards starting at segment 26 of the satellite ground track.

Figure 9c gives an example of co-geolocated ground tracks, with the airborne tracks on the left and the satellite ground track on the right (note that segment numbering is computed automatically and independently for each data set). The tracks in this section have an average spacing of about 18 m. The underlying Planet SkySat image, which was collected on 18 August 2019, only 5 days after flight 2 shows that the same types of crevasses are crossed by the satellite and the airborne track. Notably, with a separation of 18 m, the same crevasse provinces are crossed by the ULS tracks and the ICESat-2 tracks. This example indicates that a separation of 18 m is sufficiently small to capture the same characteristics and, specifically, function for a validation of ICESat-2 surface heights and crevasse characteristics.

7.3. Analysis of Data for RGT 450, gt1l (Strong Beam)

Predicted ICESat-2 tracks, actual ICESat-2 tracks and actual ULS flight tracks, projected to the ground, are shown in Figure 10b, plotted over a Planet SkySat image from a near-time SkySat acquisition, for beam pair 1 of RGT 450. For the strong beam (gt1l, left in Figure 10b), the ULS ground tracks are often coincide with the predicted ATLAS tracks, at the resolution of this figure. The distance between the ULS tracks and the actual ATLAS tracks is given in Figure 10c, the average distance is 18 m for the section and 20.40 m for the glacier crossing (Table 5); this distance characterizes the height comparisons. Notably, the distance between the actual and the predicted ICESat-2 track is 9.28 m (Figure 10d), which indicates that with an the 18-20m distance the track repeat capability of the airborne campaign is very good for a helicopter-based operation. Typically, repeat accuracy of satellite tracks (ATLAS actual versus ATLAS predicted) can be expected to be much better than that of a flight campaign (ULS actual versus ATLAS predicted). For the weak beam (gt1r, right set of tracks in Figure 10b, see Figure 11), the distance between actual ICESat-2 and ULS tracks is on the same order as the distance between the predicted and actual ICESat-2 tracks (and sometimes better, for example in the southern part of the plot, near 8,732,900 UTM-North).

The Planet SkySat image indicates that ULS tracks and predicted and actual ICESat-2 tracks cross the same crevasse types and in most cases the same individual crevasses. This observation is confirmed by the comparison of heights from the ULS data and ATLAS data, processed with the DDA-ice, seen in Figure 10e,f. It should be noted that the ULS operates at 905 nm (NIR), while ATLAS operates at 532 nm (green), and thus the comparison figure reflects the different penetration properties of the two altimeters, the small location differences of the ground tracks and the separation in time (the glacier moves at several meters per day in this region, because of the surge). Along-track distances of the ULS data were shifted a few meters to better align crevasses in the ULS and ATLAS data, to account for glacier movement during the separation times. Flight 2 was carried out on 13 August 2019, ATLAS data along RGT 450 were collected 27 July 2019, resulting in a 17-day time separation. Penetration differences of red and green lidars are analyzed in [21], using ICESat-2 simulator data.

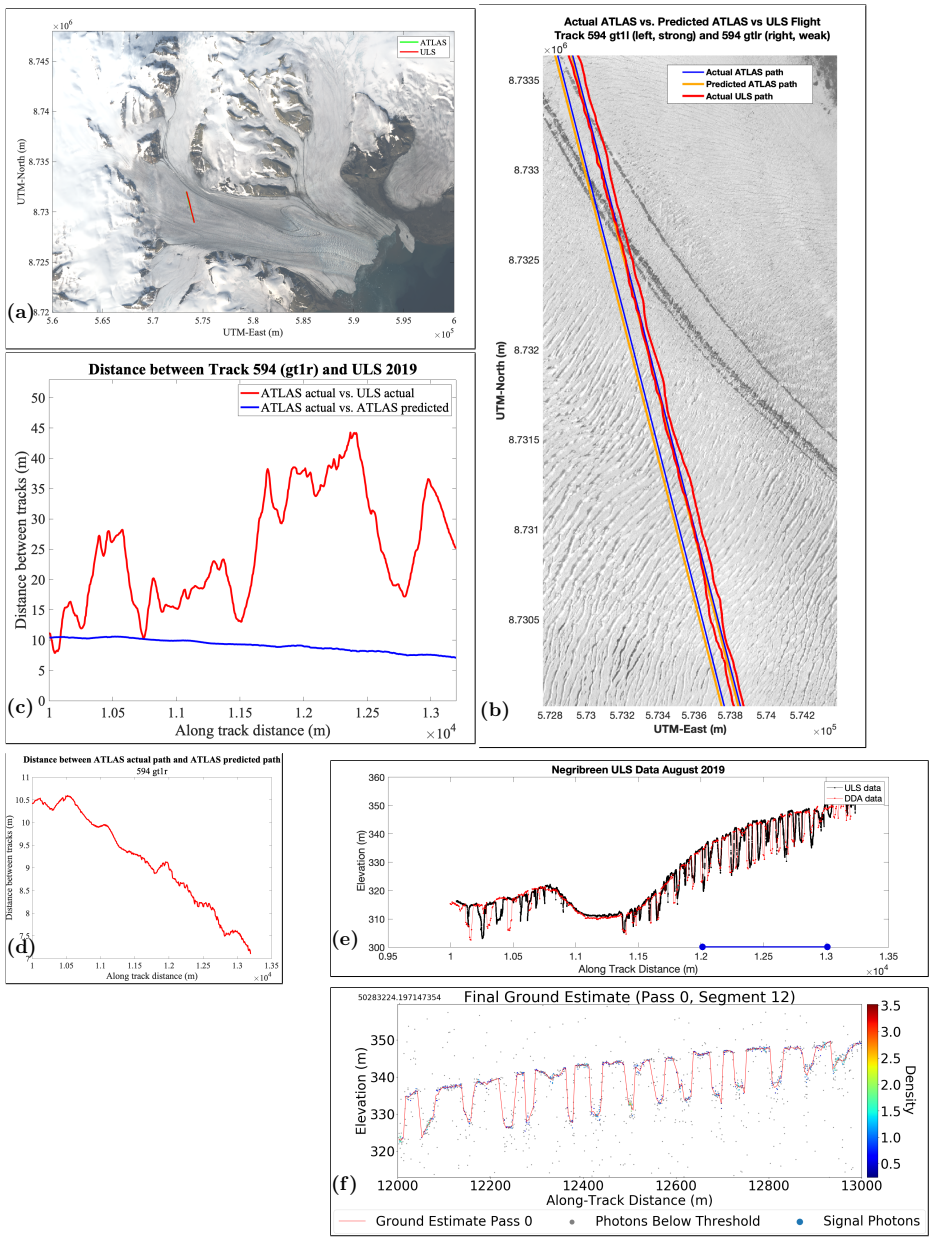

Figure 13. ICESat-2 ATLAS vs. ULS data. Track repeat accuracy and results. RGT 594, gt1r (weak), overpass 1. Negribreen validation campaign. Flight 2, 13 August 2019. (**a**) Location of DDA segments over Negribreen and closest ULS data (note the tracks are so close that the green line disappears under the red line). For segment numbering, see Figure 9 (ATLAS DDA segments). Background: Landsat-8 image from 5 August 2019 [LC08_L1TP_215003_20190805_20190820_01_T1]. Segment lengths in (**a**,**c**–**e**) are the same, segments in (**b**,**f**) are subsets. (**b**) Track separation between our ULS flight path, the ATLAS predicted flight path, and the ATLAS actual flight path for granule: [ATL03_20190805232841_05940403_002_01.h5]. Background: Planet SkySat image from 18 August 2019 [20190818_150858_ssc9_u0002_panchromatic_dn.tif]. (**c**) Separations between ATLAS Track 594 (gt1r) actual and ULS flight path, and between ATLAS Track 594 (gt1r) actual and ATLAS Track 594 (gt1r) predicted. Calculated for actual ATLAS and ULS flight paths from data shown in (**b**). (**d**) Track separation between predicted and actual ATLAS 594 (gt1r) flight paths. (**e**) ULS surface heights and ICESat-2 ATLAS DDA-ice surface heights superimposed, after GPS and IMU correction of ULS paths (ground locations). Blue line: Section covered in f. (**f**) ICESat-2 ATLAS surface heights over crevassed region derived using DDA-ice, RGT 594, gt1r, segment 12. DDA-ice parameters as in Table 2. ATL03 data set given in caption for (**c**). Rel. 03 data.

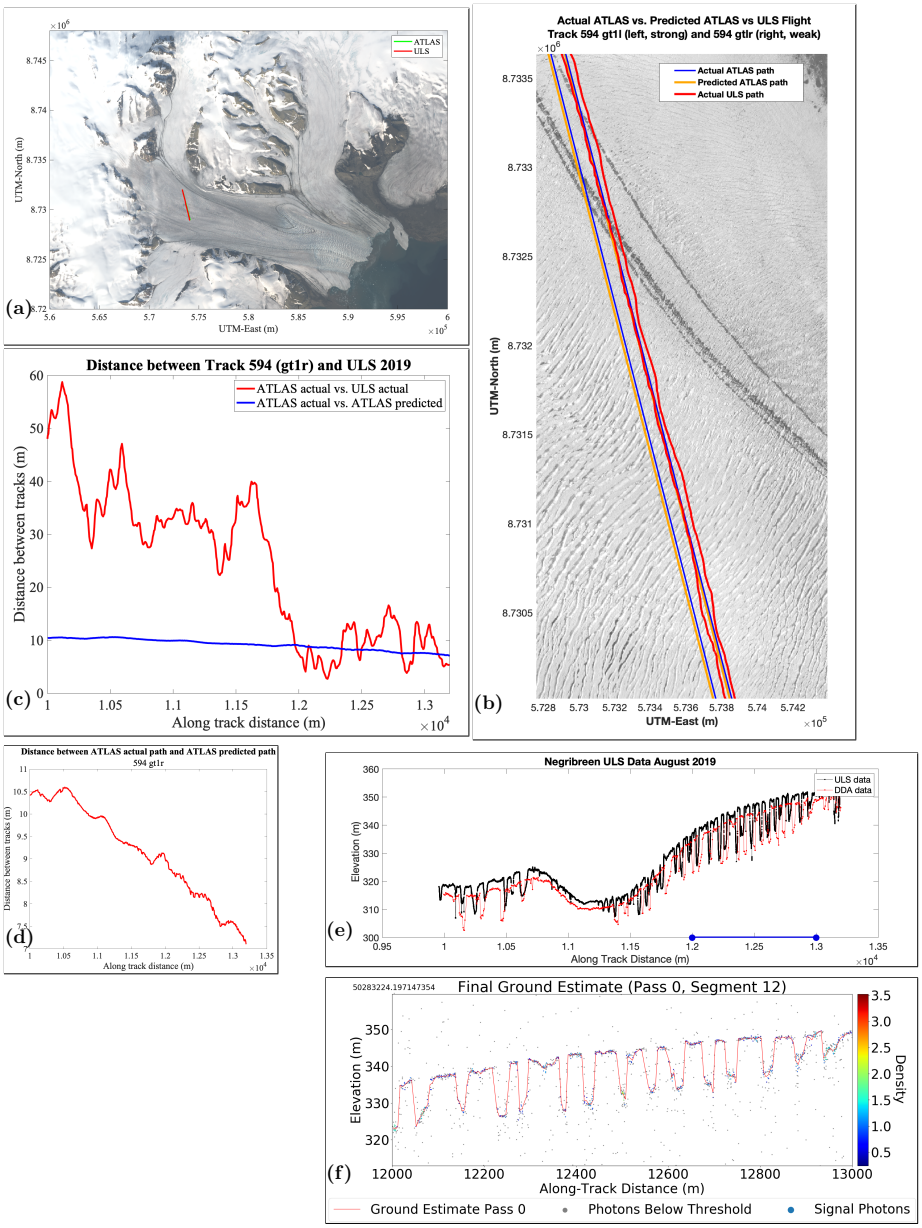

Figure 14. ICESat-2 ATLAS vs. ULS data. Track repeat accuracy and results. RGT 594, gt1r (weak), overpass 2 (high winds of 60 km/h). Negribreen validation campaign. Flight 2, 13 August 2019. (**a**) Location of DDA segments over Negribreen and closest ULS data (note the tracks are so close that the green line disappears under the red line). For segment numbering, see Figure 9 (ATLAS DDA segments). Background: Landsat-8 image from 5 August 2019 [LC08_L1TP_215003_20190805_20190820_01_T1]. Segment lengths in (**a**,**c**–**e**) are the same, segments in (**b**,**f**) are subsets. (**b**) Track separation between our ULS flight path, the ATLAS predicted flight path, and the ATLAS actual flight path for granule: [ATL03_20190805232841_05940403_002_01.h5]. Background: Planet SkySat image from 18 August 2019 [20190818_150858_ssc9_u0002_panchromatic_dn.tif]. (**c**) Separations between ATLAS Track 594 (gt1r) actual and ULS flight path, and between ATLAS Track 594 (gt1r) actual and ATLAS Track 594 (gt1r) predicted. Calculated for actual ATLAS and ULS flight paths from data shown in (**b**). (**d**) Track separation between predicted and actual ATLAS 594 (gt1r) flight paths. (**e**) ULS surface heights and ICESat-2 ATLAS DDA-ice surface heights superimposed, after GPS and IMU correction of ULS paths (ground locations). Blue line: Section covered in f. (**f**) ICESat-2 ATLAS surface heights over crevassed region derived using DDA-ice, RGT 594, gt1r, segment 12. DDA-ice parameters as in Table 2. ATL03 data set given in caption for (**c**). Rel. 03 data.

In summary, agreement of morphologies and heights is very good, and thus we conclude that the experiment setup of our airborne geophysical validation campaign serves the purpose of a validation campaign. In consequence, the resultant ICESat-2 surface heights, as calculated with the DDA-ice from the ATL03 photon data, represent the heights of the crevassed surface and the interior of the crevasses. These surface heights and crevasse morphologies are thus suited for geophysical and glaciological analyses [3]. Details in the DDA-ice results (Figure 10f) show the typical morphology of surge crevasses with relatively sharp edges to the ice surface and largely straight crevasse walls. The latter is due to the general absence of points that could define a complex crevasse walls, as are detected in the case of Jakobshav Isbræ (Ilulissat Ice Stream) crevasses [3].

7.4. Analysis of Data for RGT 450, gt1r (Weak Beam)

Figure 11 shows the same type of analyses as Figure 10, now for the weak beam of RGT 450, gt1r. For the weak beam (gt1r, right set of tracks in Figure 11b), the distance between actual ICESat-2 and ULS tracks is on the same order as the distance between the predicted and actual ICESat-2 tracks (and sometimes better, for example in the southern part of the plot, near 8,732,900 UTM-North). Average separation of the ATLAS (actual) and ULS (actual) tracks for this glacier crossing is only 11.32 m. In this case, the distance to the predicted tracks is larger than to the actual tracks. As in the previous example (Figure 10), along-track distances were shifted to account for the 17-day time separation between ATLAS and ULS data along the RGT 450 track.

All conclusions regarding evaluation capabilities hold as stated for the example of the RGT 450 strong beam. In conclusion, we are able to validate the ICESat-2 ATLAS surface-height determination capability for the weak beam as well, with exemplary results over crevassed terrain shown in Figure 11f.

7.5. Analysis of Data for RGT 594, gt1l (Strong Beam)

Figure 12 presents the results of RGT 594 with its characteristics surge crevasses, with clear-cut edges, almost regular spacing and depths of 15 m (for details, see [3]). Track separation ranges from 20 m to 80 m with strong fluctuations. As the SkySat image (Figure 12b) and the comparison plot ULS-ICESat-2 indicates, crevasse provinces still line up correctly, which means that crevasses are identified where they exist.

Absolute surface heights show a difference in some paces, because of the track separation in time and location. Flight 2 was carried out on 13 August 2019, ATLAS data along RGT 594 were collected 5 August 2019, resulting in an 8-day time separation. For the example from gt1l (RGT 594), a distance-shift of ULS data was not applied, as it was not needed.

As in the example of the RGT 450 data, the ULS data for this track (RGT 594, gt1l) can be used for validation of crevasse detection and characterization of morphological types and their spatial characteristics. The crevasse profile, analyzed with the DDA-ice (Figure 12f) shows the clear-cut edges of recently opened crevasses that have not been eroded yet (where erosion and weathering would result in rounded edges, see [38]), especially in the section 2,153,000–2,153,600 m along-track distance. In contrast, the remainder of the profile segment 23 shows eroded crevasses (2,153,600–2,154,000). This example also indicates that relative dating of crevasse opening may be possible using ATLAS data and the DDA-ice.

7.6. Analysis of Data for RGT 594, gt1r (Weak Beam), Overpass 1

In this example, we find a close match of individual crevasses, in addition to the match of spatial crevasse characteristics. Notably this best matching of crevasses between ULS and ICESat-2 data exists for a track with separation of 10 to 45 m, and the locations of lowest separation do not line up with locations of best crevasse matches between the two instruments, airborne and satellite altimeters (Figure 13c). DDA-ice surface heights over crevassed terrain are retrieved correctly for the weak beam in this case as well. The results of the DDA-ice analysis (Figure 12f) show the typical square-cut blocky profile of a field

of recently opened crevasses. Remarkably this type of morphological detail is reflected in the ATLAS data and their analysis. A distance shift was applied to the ULS data, to align crevasse morphologies with those in the ATLAS RGT 594 gt1r (weak beam) data.

7.7. Analysis of Data for RGT 594, gt1r (Weak Beam), Overpass 2

The plan for overpass 2 was to underfly the strong beam again, but we ended up closer to the weak beam, for which analyses are presented (Figure 14). During this part of the experiment, the helicopter drifted in high winds from the track location of the strong beam to that of the weak beam, ending up within 10 m from the weak beam. The ULS-ICESat-2 comparison has a larger apparent error than for overpass 1 of the same track. This is most likely attributable to an increased error in the IUM correction, due to larger and more variable IMU values during high winds, which in turn was caused by more helicopter attitude changes than during the earlier parts of flight 2.

As seen in Figure 14e, the crevasse characteristics are similar, despite the existing offset in absolute surface height values between ULS and ATLAS data. This example demonstrates particularly well that a crevasse characterization based on surface-roughness analysis is more robust than absolute surface-height determination.

8. Results Part 4: Track-Repeat Accuracies (ULS versus ICESat-2 ATLAS-Predicted and ATLAS-Actual)

The "actual" and "predicted" track repeat capabilities of our experiment setup are summarized in Table 5, which gives the average distances between (a) the ATLAS-predicted and the ATLAS-actual tracks and (b) the ATLAS-actual and ULS-actual tracks.

By design of the experiments, we aimed to repeat the predicted ATLAS tracks, which are based on the RGTs and the type of ATLAS track available during the flight experiments. The track-repeat capability for predicted ATLAS ground tracks is typically 18–20 m; this distance characterizes the combined capability of flight planning, helicopter flights in changing weather conditions and GPS and IMU corrections to underfly a (planned/ predicted) satellite track. Notably, the distance between predicted and actual ATLAS ground tracks has an average of 6.51 m to 15.65 m, with approximately 9 m for three out of five case studies. Therefore the track repeat distance between airborne and predicted satellite tracks (repeat capability) is only twice as large as the ATLAS-predicted to ATLAS-actual tracking capability, which is an impressive value for helicopter-based experiments.

The distance that characterizes the height comparisons between the ULS data and the ATLAS surface heights is the distance between actual-ATLAS and ULS (actual) ground tracks. Average distances between ATLAS-actual and ULS ground tracks is generally better than 25 m, with a minimum of 11.32 m and an outlier of 60 m track separation. In a kinematic experiment, it is not possible to achieve the co-locational accuracy of a static experiment, and observation of surface heights and crevasses on a surging glacier is not feasible (it is dangerous). The distances that we have achieved are sufficiently small to allow the surface-height validation.

It is sometimes, but not always, possible to match the location and height of individual crevasses. The next section will focus on the surface-height comparison and the role of summative quantitative characteristics, as well as on crevasse morphology.

9. Results Part 5: Comparison of Surface Heights and Crevasse Characteristics from ULS and ICESat-2 ATLAS Data. Surface Roughness

9.1. Surface Heights and Crevasse Morphologies

The numerical evaluation of of ICESat-2 surface heights, compared to heights from airborne observations, is carried out by an analysis of spatial surface structures, here crevasse characteristics (analysis of spatial surface roughness), rather than by point-wise height differencing. The primary reason for this approach to evaluation is that the evolution of the surge, and of glacial acceleration in general, is captured in crevasse characteristics. Comparison of absolute surface heights is less meaningful, for the following three reasons: (1) Due to the surge, the glacier moves at 1–2 m per day in the survey area in upper

Negribreen, according to a velocity analysis based on Sentinel-1 SAR data (Figure 4a) of the European Space Agency's (ESA's) Copernicus Mission. (2) There is a spatial track separation of zero to typically 20-25 m between the actual ATLAS ground tracks and the ULS ground tracks (see, Table 5) over a sloping glacier. (3) Time separation between flight 2 (13 August 2019) and ICESat-2 ATLAS data collection is 8 days for RGT 594 (5 August 2019) and 17 days for RGT450 (27 July 2019). Depending on track orientation, slope and velocity vector, these factors can cancel each other out or increase actual surface height differences.

Planet SkySat imagery was collected to support the ICESat-2 validation objective and the study of the surge. Comparison with a Planet SkySat image from 18 August 2019 (only 5 days after flight 2 on 13 August 2019) supports the finding that the same crevasse types are observed in the ULS data and ICESat-2 ATLAS data for all glacier crossings of our validation experiments. This matches the result from the analysis of track distances (Result Part 4, Section 8). Comparisons of ULS surface-height profiles and ATLAS surface-height profiles show the same characteristics with respect to presence/absence of crevasse fields, crevasse morphologies and crevasse spacing (for the latter, see Section 9.2). The crevasse profiles, analyzed with the DDA-ice, clearly show the clear-cut edges of recently opened surge crevasses in some fresh crevasse fields, contrasting to older crevasses that have been eroded by weathering, melting and snow deposition.

Differences in absolute height of the ice-surface between crevasses are attributed to the separation distance of the tracks over a sloping glacier and to the surge-related fast movement of the glacier during to the time separation between the airborne and satellite observations. Along-track distances were shifted a few meters to better align crevasses in the ULS and ATLAS data, in some experiments, to account for glacier movement between the times of the airborne experiments (13 August 2019) and ICESat-2 data collection (RGT 450: 27 July 2019, 17-day separation; RGT 594: 5 August 2019, 8-day separation). The ULS operates at 905 nm, which yields different penetration characteristics especially in slush and water.

The detail of the ICESat-2 DDA-ice surface heights in crevassed and smooth terrain and the comparison to airborne data indicates that surface heights, measured by ICESat-2, are accurately represented in the DDA-ice analysis.

9.2. Crevasse Spacing, Crevasse Depth and Surface Roughness

Crevasse spacing and depths for ATLAS segment 23 (RGT 594 gt1l) (Figure 11f) and matching ULS data are characterized by the values in the following table (Table 6), cited after [3]. These values match well, considering that the green light (532 nm) of the ATLAS sensor and the NIR light (905 nm) of the ULS have different penetration depths into snow, firn and slush and thus interact differently with the cryospheric materials at the bottom of the crevasses.

Table 6. Crevasse spacing and depths for Negribreen evaluation profile "segment 23 (RGT 594) 5 August 2019". Comparison of results from ULS airborne laser altimeter data and DDA-ice applied to ICESat-2 ATLAS data ATL03_20190805232841_05940403_002_01.h5. (From [3], Table 3).

	Mean Crevasse Spacing (m)	Maximum Crevasse Depth (m)	Mean Crevasse Depth (m) (>5 m)
DDA-ice	52.12	16.01	10.95
ULS	58.82	13.96	10.18

Surface roughness is analyzed for both the ULS data and the DDA-ice ATLAS surface heights, employing the $pond_{res}$ parameter of geostatistical characterization [31,39,40].

The $pond_{res}$ parameter is defined as the maximal value of the first-order residual vario function. First-order vario functions are used to mathematically summarize the spatial surface roughness in a given area. Vario functions are defined in a discrete mathematics framework, formally akin to the variogram of geostatistics (which requires the assumption that the data set may be considered a realization of a spatial random function that satisfies

the intrinsic hypothesis [41,42]). Other than the variogram, vario functions exist always, which makes them particularly useful for applications in computational geosciences. The first-order vario function is defined as follows [31,39]:

$$v_1(h) = \frac{1}{2n}\sum_{i=1}^{n}[z(x_i) - z(x_i + h)]^2 \tag{3}$$

for pairs of points $(x_i, z(x_i)), (x_i + h, z(x_i + h)) \in \mathcal{D}$, where $\mathcal{D}$ is a region in $\mathcal{R}^2$ (case of survey profiles) or $\mathcal{R}^3$ (case of survey areas) and n is the number of pairs separated by h; the distance value h is also termed "lag". The function $v_1(h)$ is called the *first-order vario function*. This function exists always and has a finite value. In situations where a regional trend underlies the data, the residual vario function is often more useful to analyze roughness than the vario function. Using

$$m(h) = \frac{1}{n}\sum_{i=1}^{n}[z(x_i) - z(x_i + h)], \tag{4}$$

the residual vario function is defined as:

$$res_1(h) = v_1(h) - \frac{1}{2}m(h)^2. \tag{5}$$

The results of the roughness analysis using the $pond_{res}$ parameter are shown in Figure 15, overlain on the Planet SkySat image. Surface roughness characteristics of both ATLAS and ULS surface profiles line up with the location of crevasse fields.

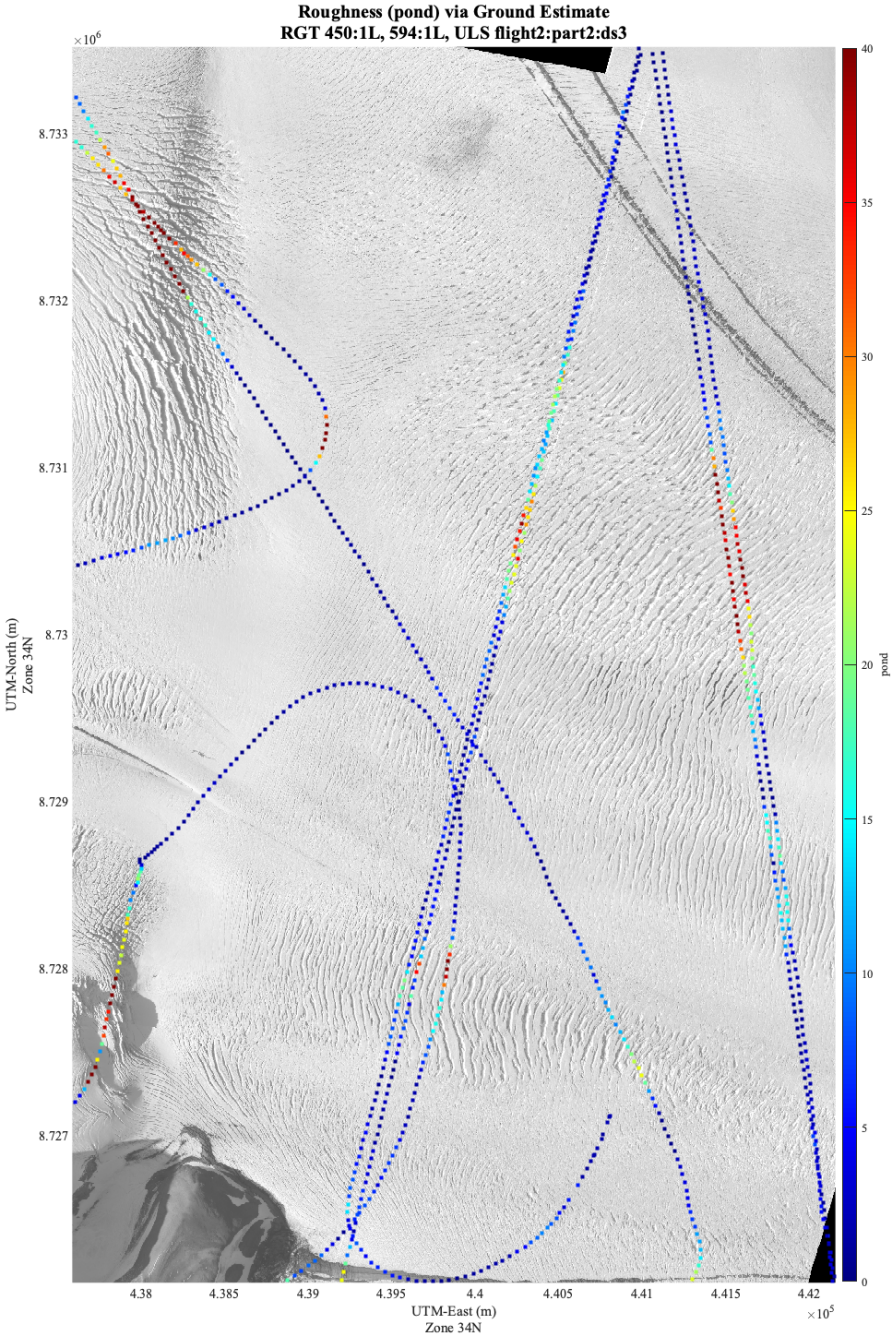

Figure 15. Ice-surface roughness in upper Negribreen during surge in 2019, from airborne altimeter data (ULS) data and ICESat-2 ATLAS Data, compared to Planet SkySat image data. ICESat-2 ATLAS Granules: [ATL03_20190805232841_05940403_002_01.h5] [RGT 594 gt1l 5 August 2019] and [ATL03_20190727132129_04500405_002_01.h5] [RGT 450 gt1l]. SkySat Image [20190818_150858_ssc9_u0002_panchromatic_dn.tif]. SkySat ssc9 data have 0.72 m pixel size. Roughness measure $pond_{res}$ calculated for ICESat-2 ATLAS data, analyzed with the DDA-ice, and for ULS data. ICESat-2 RGT594 and matching ULS tracks are the right almost straight set; ICESat-2 RGT450 and matching ULS tracks are the left almost straight sets. For RGT 594, the airborne track (ULS) is to the east (right) of the satellite track. For RGT 450, the airborne track and the satellite track are almost in the same location. Generally, surface roughness from parallel tracks and crossover locations matches between ICESat-2 and ULS. The $pond_{res}$ measure increases with intensity of crevassing evident in the SkySat image.

10. Summary and Conclusions

The topic of this paper is the airborne evaluation of ICESat-2 Advanced Topographic Laser Altimeter System (ATLAS) measurement capabilities and surface-height-determination over crevassed glacial terrain, with a focus on the geodetical accuracy of geophysical data collected from a helicopter. Negribreen, Svalbard, during surge in 2019 provided an ideal situation for the validation of ICESat-2 ATLAS measurements and surface height-determination over crevassed and otherwise complex ice surfaces, using the the density-dimension algorithm for ice surfaces (DDA-ice). As a result of the ongoing surge, different types of morphologically complex ice surface types, including many different types of wet and dry crevasses, were found in close proximity. Airborne geophysical data were collected during two campaigns in summers of 2018 and 2019. Airborne experiment setup, geodetical correction and data processing steps are described in this study, focussing on the 2019 data in the correction steps.

Experiment setup. The experiment setup consisted of a suite of small geophysical instruments mounted on a helicopter (an AS-350 "Eurocopter"), a LaserTech Universal Laser System (ULS) (a laser profilometer operating at 905 nm frequency), a Global Positioning System (GPS) receiver for collection of kinematic "rover" data, an Inertial Measurement Unit (IMU) for collection of attitude data of the platform and a GoPro Hero 5 for recording of on-board-time-lapse imagery. A GPS base station was placed on the side of the glacier for each flight experiment (and collected at the end of the flight). Photographs from handheld cameras complemented the surveys. Flight tracks of the airborne experiments were planned to repeat predicted ATLAS ground tracks, which are calculated based on the ICESat-2 Reference Ground Tracks (RGTs) and the only type of track data available prior to ICESat-2 overpasses. Following ICESat-2 data collection, actual ATLAS ground tracks become available after a few weeks following detailed geodetical correction. Planet SkySat data (0.72 m pixel size) were collected to support the validation campaign, the imagery closest in time to the 2019 flights stems from 8 August 2019 and has a 5-day separation to the 2019 flight data analyzed here.

ICESat-2 ATLAS Algorithm: DDA-ice. To obtain surface heights over crevassed and otherwise complex ice surfaces, ICESat-2 data are analyzed using the density-dimension algorithm for ice surfaces (DDA-ice). The DDA-ice is an algorithm that was specifically designed for the analysis of micro-pulse photon-counting laser altimeter data as collected by ATLAS. The DDA-ice utilizes the radial basis function for data aggregation into a density field, which adds a dimension, and an auto-adaptive threshold function for separation of signal from background. The DDA-ice yields surface heights at the nominal 0.7 m along-track spacing of ATLAS data (under clear-sky atmospheric conditions) and 2.5 m piece-wise linear interpolated surface heights and crevasse morphologies. In that this paper substantiates the geodetical results and provides detailed and accurate information of the validation campaign, the results here further validate the surface-height determination over crevassed and otherwise morphologically complex terrain using the DDA-ice, adding to the results reported in [3].

Geodetical Results. The study contributes to the relatively small amount of knowledge of the geodetical accuracy that can be obtained from kinematic data collection from a helicopter and thus may be of interest for future airborne satellite validation campaigns. We analyzed and compared the geodetical accuracy of (a) kinematic GPS data, collected by a rover on a helicopter and a base station on the side of the glacier, corrected in post-processing, (b) real-time kinematic (RTK) GPS data, where the updated position is calculated during flight and communicated to the pilot for adjustment of the flight track, and (c) kinematic GPS data, collected by a rover and post-processed without using base-station data. Findings of our study regarding these different GPS-data collection and correction modes include the following: (1) Kinematic GPS data collection with correction in post-processing yields higher accuracies than RTK data collection, because the frequent adjustments of the flight tracks lead to inaccuracies that more than offset the across-track distances resultant from straight lines flown across the glacier. (2) Processing of only the

rover data using the Natural Resources Canada Spatial Reference System Precise Point Positioning (CSRS-PPP [34]) software is sufficiently accurate for the sub-satellite validation purpose of our study. (3) Distances between ICESat-2 ground tracks and airborne ground tracks were generally better than 25 m, while distances between predicted and actual ICESat-2 ground track were on the order of 9 m, which allows direct comparison of ice-surface heights and spatial statistical characteristics of crevasses from the satellite and airborne measurements.

Capability for track repeat ranges from an average of 11.32 m to 24.87 m for the distance between ICESat-2 ATLAS-actual and ULS (actual) ground tracks, with an outlier of 60 m. Differences between ICESat-2 ATLAS-predicted ground tracks (based on the RGTs) and ATLAS-actual ground tracks (determined after ICESat-2 data collection and geodetical correction) range from 6.51 m to 15.65 m for the average difference of a glacier crossing, with an approximately 9 m average difference as the most common value in the experiments in our study.

Technical Measurement Results. Following geodetical correction, the 2019 airborne campaign data over Negribreen are analyzed with respect to measurement accuracies and precisions. (4) The Lasertech Universal Laser System (ULS), operated at up to 300 m above ground level, yields full return frequency (400 Hz) and 0.06–0.08 m on-ice along-track spacing of height measurements. (5) Cross-over differences of airborne laser altimeter data are -0.172 ± 2.564 m along straight paths over generally crevassed terrain, which implies a precision of approximately 2.6 m for ICESat-2 validation experiments. (6) In summary, the comparatively light-weight experiment setup of a suite of small survey equipment mounted on a Eurocopter (Helicopter AS-350) and kinematic GPS data analyzed in post-processing using CSRS-PPP leads to high-accuracy repeats of ICESat-2 tracks.

Comparison of Surface Heights and Crevasse Characteristics from ULS and ICESat-2 ATLAS Data. Surface Roughness. As a result of the geodetical analysis and the technical measurement analysis, the data collected during the Negribreen airborne geophysical validation campaigns can be utilized for validation of ICESat-2 ATLAS data, analyzed with the DDA-ice. A detailed analysis of airborne and satellite data for and from RGT 450 and RGT 594, which cross different crevasse provinces in upper Negribreen, is presented. The analysis includes data from the weak beam and the strong beam of ATLAS (which differ in strength of the transmitted laser signal by a factor of 4) and a repeat experiment for one beam.

It is often, but not always, possible to match individual crevasses between the airborne height data and the ICESat-2 data. Differences are caused by the fast movement of the glacier combined with the distance between the airborne and satellite ground tracks. Instead of obtaining an always perfect match between individual crevasses, the morphological characteristics of a crevasse field are ultimately the objective of observation and analysis. Therefore, the comparison between airborne ULS data and ICESat-2 ATLAS data includes surface heights, crevasse spacing and depth, crevasse morphology (shape of the crevasse profile) and surface roughness. All parameters are found to be in good agreement. In conclusion, ICESat-2 surface heights, determined with the DDA-ice, are suitable for geophysical studies of fast-moving glaciers and glacial acceleration, especially surging.

Geophysical conclusions. The glaciological motivation for collection of data over a surge glacier is the investigation of the surge itself, including the evolution of the ice dynamics, glacial hydrology, surface height changes and mass transfer within the glacier system, as well as calving leading to mass transfer from the glacier system to the ocean as a contributing factor to sea-level change. In all of these contexts, the morphological characteristics of crevasse fields and ice fronts are more relevant than measurements of individual crevasse shapes. The validation of surface height measurements in this study supports the finding that the morphological characteristics, including crevasse depth, spacing and surface roughness of crevassed and uncrevassed areas, are in close agreement between the airborne and the satellite data (when analyzed with the DDA-ice). The latter finding was already reported in [3], this paper provides the geodetical substantiation of the

geophysical results in the referenced paper and a larger base of analyzed examples from the field experiments. This paper is also a validation of the capabilities of the DDA-ice to identify crevasses and complex morphological shapes in ICESat-2 ATLAS data.

The final result of the validation is that ICESat-2 ATLAS data, analyzed with the DDA-ice, facilitate surface-height determination over crevassed terrain, in good agreement with airborne data, including spatial characteristics, such as surface roughness, crevasse spacing and depth, which are key informants on the deformation and dynamics of a glacier during surge.

Author Contributions: U.C.H. designed the study, carried out part of the analysis and wrote the paper. M.L. and T.T. carried out most of the data analysis and contributed to writing the paper. T.N. carried out an essential part of the GPS data analysis and contributed to writing the paper. All authors have read and agreed to the published version of the manuscript.

Funding: Research and data collection were supported by the U.S. National Aeronautics and Space Administration (NASA) Earth Sciences Division under awards 80NSSC20K0975, 80NSSC18K1439 and NNX17AG75G and by the U.S. National Science Foundation (NSF) under awards OPP-1745705 and OPP-1942356 (Principal Investigator for all awards: Ute Herzfeld). The data collection was also partly supported through a 2018 Access Pilot Project (2017_0010) of the Svalbard Integrated Observing System (SIOS). All this support is gratefully acknowledged.

Institutional Review Board Statement: Not applicable.

Informed Consent Statement: Not applicable.

Data Availability Statement: (1) ICESat-2 data products are available under https://earthdata.nasa.gov/ (accessed 3 October 2021) provided by the National Snow and Ice Data Center (NSIDC). The ICESat-2 ATLAS data product ATL03, and any other ICESat-2 ATLAS data product cited in this paper, can be identified by their digital object identifiers (dois), as given in the references. (2) Data collected as part of the Negribreen Airborne Geophysical Campaigns, collected by the first author and her team, in 2018 are available through the NSF Arctic Data Center and can be accessed at https://arcticdata.io/data/10.18739/A2QF8JK7T/ (accessed on 3 October 2021). The data sets are referenced as follows: Ute Herzfeld and Thomas Trantow, Airborne Laser Altimeter, Global Positioning System (GPS), Inertial Measurement Unit (IMU) and Imagery Campaign of the Surging Negribreen Glacier, Svalbard, in July 2017 and July 2018. Arctic Data Center, doi:/data/10.18739/A2QF8JK7T. The project landing page is: https://arcticdata.io/catalog/view/doi%3A10.18739%2FA2QF8JK7T (accessed on 3 October 2021). (3) Planet SkySat data are in the process of becoming available through the NASA Commercial SmallSat Data Acquisition Project (CSDAP) https://earthdata.nasa.gov/esds/csdap (accessed on 3 October 2021). Results from the Pilot Project of the first author are included in the Report, accessible at https://cdn.earthdata.nasa.gov/conduit/upload/14180/CSDAPEvaluationReport_Apr20.pdf (accessed on 3 October 2021) (4) Landsat-8 data are freely available through the U.S. Geological Survey, see https://www.usgs.gov/core-science-systems/nli/landsat/landsat-data-access?qt-science_support_page_related_con=0#qt-science_support_page_related_con (accessed on 3 October 2021) Landsat data products held in the USGS archives can be searched and downloaded at no charge from a variety of data portals. This page provides information about accessing Landsat Collection 2 and Landsat Collection 1 Level-1 and Level-2 data products (as quoted from the cited webpage).

Acknowledgments: Thanks are due to colleagues and staff at SIOS, NPI, UNIS and Airlift and captain and crew of R/V Lance, especially to our pilots and technicians Anders Bjørghum, Gunnar Nordahl, Tor Andre Vaksdal, Harald Sandal and Gustav Svanström (Airlift), to Jack Kohler, Havard Hansen, Harvey Goodwin, Geir Ove Aspnes, Jørn Dybdahl, Norwegian Polar Institute, and Chris Borstad, University Centre in Svalbard (UNIS), now University of Montana, to Inger Jennings and Heikki Lihavainen (SIOS), to Kristin Woxholth, Longyearbyen, for help with logistical support, to the ICESat-2 Project, especially Thomas Neumann, Kaitlin Harbeck, David Hancock and Anthony Martino for collaboration and support regarding ICESat-2, to Annie Zaino, Joe Pettit, Spencer Niebuhr (UNAVCO Boulder) for help with GPS data collection and correction, to Brian Donahue, Canadian Geodetic Survey, for information on CSRS-PPP to Compton Tucker and Manil Maskey (NASA) and Paris Good, Planet, for coordination of SkySat data acquisition under the NASA Commercial SmallSat Data Acquisition Project (CSDAP), to Laurie Padman and Susan Howard (Earth&Space Research, Corvallis, Oregon) for comments on the study, and to Connor Myers and Sam Bennetts,

Geomathematics Group, University of Colorado Boulder, for assistance with data collection over Negribreen in 2018 and 2017, respectively, and last not least to Shridhar Jawak, UNIS, Longyearbyen, Svalbard for inviting us to contribute to the Virtual Remote-Sensing Conference. The helicopter was provided by the Norwegian Polar Institute and operated by Airlift. Collection of airborne data was conducted with permission of the National Security Authority of Norway, the Civil Aviation Authority of Norway and the Governor of Svalbard, registered as Research in Svalbard Project RIS-10827 "NEGRIBREEN SURGE" (2017–2019). All this support is gratefully acknowledged.

Conflicts of Interest: The authors declare no conflict of interest.

References

1. Markus, T.; Neumann, T.; Martino, A.; Abdalati, W.; Brunt, K.; Csatho, B.; Farrell, S.; Fricker, H.; Gardner, A.; Harding, D.; et al. The Ice, Cloud, and land Elevation Satellite-2 (ICESat-2): Science requirements, concept, and implementation. *Remote. Sens. Environ.* **2017**, *190*, 260–273. [CrossRef]
2. Neumann, T.A.; Martino, A.J.; Markus, T.; Bae, S.; Bock, M.R.; Brenner, A.C.; Brunt, K.M.; Cavanaugh, J.; Fernandes, S.T.; Hancock, D.W.; et al. The Ice, Cloud, and Land Elevation Satellite–2 mission: A global geolocated photon product derived from the Advanced Topographic Laser Altimeter System. *Remote. Sens. Environ.* **2019**, *233*, 111325. [CrossRef] [PubMed]
3. Herzfeld, U.; Trantow, T.; Lawson, M.; Hans, J.; Medley, G. Surface heights and crevasse types of surging and fast-moving glaciers from ICESat-2 laser altimeter data—Application of the density-dimension algorithm (DDA-ice) and validation using airborne altimeter and planet skysat data. *Sci. Remote. Sens.* **2021**, *3*, 100013. [CrossRef]
4. Schutz, B.; Zwally, H.; Shuman, C.; Hancock, D.; DiMarzio, J. Overview of the ICESat Mission. *Geophys. Res. Lett.* **2005**, *32*. [CrossRef]
5. Zwally, H.; Schutz, B.; Abdalati, W.; Abshire, J.; Bentley, C.; Brenner, A.; Bufton, J.; Dezio, J.; Hancock, D.; Harding, D.; et al. ICESat's laser measurements of polar ice, atmosphere, ocean, and land. *J. Geodyn.* **2002**, *34*, 405–445. [CrossRef]
6. Stocker, T.F.; Qin, H.; Plattner, G.-K.; Tignor, M.; Allen, S.K.; Boschung, J.; Nauels, A.; Xia, Y.; Bex, V.; Midgley, P.M.E. *Climate Change 2013: The Physical Science Basis. Contribution of Working Group I to the Fifth Assessment Report of the Intergovernmental Panel on Climate Change*; Cambridge University Press: Cambridge, UK, 2013.
7. Herzfeld, U.C.; Mayer, H. Surge of Bering Glacier and Bagley Ice Field, Alaska: An update to August 1995 and an interpretation of brittle-deformation patterns. *J. Glaciol.* **1997**, *43*, 427–434. [CrossRef]
8. Herzfeld, U.C.; McDonald, B.; Wallin, B.F.; Krabill, W.; Manizade, S.; Sonntag, J.; Mayer, H.; Yearsley, W.A.; Chen, P.A.; Weltman, A. Elevation changes and dynamic provinces of Jakobshavn Isbræ, Greenland, derived using generalized spatial surface roughness from ICESat GLAS and ATM data. *J. Glaciol.* **2014**, *60*, 834–848. [CrossRef]
9. Mayer, H.; Herzfeld, U. Structural glaciology of the fast-moving Jakobshavn Isbræ, Greenland, compared to the surging Bering Glacier, Alaska, USA. *Ann. Glaciol.* **2000**, *30*, 243–249. [CrossRef]
10. Mayer, H.; Herzfeld, U. A structural segmentation, kinematic analysis and dynamic interpretation of Jakobshavns Isbræ, West Greenland. *Z. Gletsch. Glazialgeol.* **2001**, *37*, 107–124.
11. Trantow, T.; Herzfeld, U.C. Crevasses as indicators of surge dynamics in the Bering Bagley Glacier System, Alaska: Numerical experiments and comparison to image data analysis. *J. Geophys. Res. Earth Surf.* **2018**, *123*, 1615–1637. [CrossRef]
12. Herzfeld, U.; Trantow, T.; Bennetts, S. Surge-forced structural disintegration, enhanced calving and resultant rapid mass loss of a large Arctic fjord glacier (Negribreen, Svalbard). *GRL* **2018**, *submitted*.
13. Murray, T.; Strozzi, T.; Luckman, A.; Jiskoot, H.; Christakos, P. Is there a single surge mechanism? Contrasts in dynamics between glacier surges in Svalbard and other regions. *J. Geophys. Res.* **2003**, *108*, 2237. [CrossRef]
14. Smith, B.; Fricker, H.; Gardner, A.; Siegfried, M.; Adusumilli, S.; Csatho, B.; Holschuh, N.; Paolo, F. *ICESat-2 L3a Land Ice Height, Version 3*; NASA ICESat-2 Project; NASA: Boulder, CO, USA, 2020. [CrossRef]
15. Smith, B.; Hancock, D.; Harbeck, K.; Roberts, L.; Neumann, T.; Brunt, K.; Fricker, H.; Gardner, A.; Siegfried, M.; Adusumilli, S.; et al. *ICESat-2 Algorithm Theoretical Basis Document for Land Ice Along-Track Height Product, February 20, 2020*; NASA ICESat-2 Project; NASA: Greenbelt, MD, USA, 2020; 107p. [CrossRef]
16. Brunt, K.M.; Smith, B.E.; Sutterly, T.C.; Kurtz, N.T.; Neumann, T.A. Comparisons of Satellite and Airborne Altimetry With Ground-Based Data From the Interior of the Antarctic Ice Sheet. *Geophys. Res. Lett.* **2020**, *48*, e2020GL090572. [CrossRef]
17. Cui, H.; Li, R.; Li, H.; Hao, T.; Qiao, G.; He, Y.; Hai, G.; Xie, H.; Cheng, Y.; Li, B. Field validation of ICESat-2 data along CHINARE Route in East Antarctica. In *The International Archives of the Photogrammetry, Remote Sensing and Spatial Information Sciences*; XLIII-B3-2021 (XXIV ISPRS Congress); Copernicus: Göttingen, Germany, 2021; pp. 443–448. [CrossRef]
18. Neumann, T.; Brenner, A.; Hancock, D.; Robbins, J.; Saba, J.; Harbeck, K.; Gibbons, A.; Lee, J.; Luthcke, S.; Rebold, T. *ICESat-2 Algorithm Theoretical Basis Document for Global Geolocated Photons, 15 October 2019*; NASA ICESat-2 Project; NASA: Greenbelt, MD, USA, 2019; 202p. [CrossRef]
19. Neumann, T.; Brenner, A.; Hancock, D.; Robbins, J.; Saba, J.; Harbeck, K.; Gibbons, A.; Lee, J.; Luthcke, S.; Rebold, T. *ATLAS/ICESat-2 L2A Global Geolocated Photon Data, Version 3*; NASA ICESat-2 Project; NASA: Greenbelt, MD, USA, 2020. [CrossRef]
20. Magruder, L.; Neumann, T.; Kurtz, N. ICESat-2 early mission synopsis and observatory performance. *Earth Space Sci.* **2021**, *8*, e2020EA001555. [CrossRef]

21. Herzfeld, U.; Trantow, T.; Harding, D.; Dabney, P. Surface-height determination of crevassed glaciers—Mathematical principles of an Auto-Adaptive Density-Dimension Algorithm and validation using ICESat-2 Simulator (SIMPL) data. *IEEE Trans. Geosci. Remote. Sens.* **2017**, *55*, 1874–1896. [CrossRef]
22. Luthcke, S.B.; Pennington, T.; Rebold, T.; Thomas, T. *Algorithm Theoretical Basis Document (ATBD) for ATL03g ICESat-2 Receive Photon Geolocation, 28 October 2019*; NASA ICESat-2 Project; NASA: Greenbelt, MD, USA, 2019; 63p.
23. Luthcke, S.; Zelensky, N.; Rowlands, D.; Lemoine, F.; Williams, T. The 1-centimeter orbit: Jason-1 precision orbit determination using gps, slr, doris, and altimeter data special issue: Jason-1 calibration/validation. *Mar. Geod.* **2003**, *26*, 399–421. [CrossRef]
24. Petit, G.; Luzum, B. *IERS Conventions (2010) IERS*; Technical Note No. 36; International Earth Rotation and Reference Systems Service: Frankfurt, Germany, 2010.
25. Dabney, P.W.; Harding, D.J.; Abshire, J.; Huss, T.; Jodor, G.; Machan, R.; Marzouk, J.; Rush, K.; Seas, A.; Shuman, C.; et al. The Slope Imaging Multi-polarization Photon-counting Lidar: Development and performance results. In *Geoscience and Remote Sensing Symposium (IGARSS), 2010 IEEE International*; IEEE: Piscataway, NJ, USA, 2010; pp. 653–656. Available online: http://ieeexplore.ieee.org/xpls/abs_all.jsp?arnumber=5650862 (accessed on 3 October 2021).
26. Harding, D.; Dabney, P.; Valett, S.; Yu, A.; Vasilyev, A.; Kelly, A. Airborne polarimetric, two-color laser altimeter measurements of lake ice cover: A pathfinder for nasa's icesat-2 spaceflight mission. In *Geoscience and Remote Sensing Symposium (IGARSS), 2011 IEEE international*; IEEE: Piscataway, NJ, USA, 2011; pp. 3598–3601.
27. Palm, S.; Yang, Y.; Herzfeld, U. *ICESat-2 Algorithm Theoretical Basis Document for the Atmosphere, Part I: Level 2 and 3 Data Products, February 14, 2020*; NASA ICESat-2 Project; NASA: Greenbelt, MD, USA, 2020; 104p. [CrossRef]
28. Palm, S.; Yang, Y.; Herzfeld, U.; Hancock, D.; Barbieri, K.; Wimert, J. *ATLAS/ICESat-2 L2A Normalized Relative Backscatter Profiles, Version 3*; NASA ICESat-2 Project; NASA: Greenbelt, MD, USA, 2020. [CrossRef]
29. Neumann, T.; Brenner, A.; Hancock, D.; Robbins, J.; Saba, J.; Harbeck, K.; Gibbons, A.; Lee, J.; Luthcke, S.; Rebold, T. *ICESat-2 Algorithm Theoretical Basis Document for Global Geolocated Photons, April 2020*; NASA ICESat-2 Project; NASA: Greenbelt, MD, USA, 2020; 207p. [CrossRef]
30. Crocker, R.I.; Maslanik, J.A.; Palo, S.E.; Adler, J.J.; Herzfeld, U.C.; Emery, W.J. A sensor package for ice surface characterization using small unmanned aircraft systems. *IEEE Trans. Geosc. Remote Sens.* **2011**, *49*, 1033–1047. [CrossRef]
31. Herzfeld, U.; Hunke, E.; McDonald, B.; Wallin, B. Sea Ice Deformation in Fram Strait—Comparison of CICE simulations with analysis and classification of airborne remote-sensing data. *Cold Reg. Sci. Technol.* **2015**, *117*, 19–33. [CrossRef]
32. Brodin, G.; Cooper, J.; Stevens, J. Measuring the effect of helicopter rotors on GPS reception. *Aeronaut. J. New Ser.* **2007**, *111*, 561–570. [CrossRef]
33. Banville, S.; Hassen, E.; Lamothe, P.; Farinaccio, J.; Donahue, B.; Mireault, Y.; Goudarzi, M.A.; Collins, P.; Ghoddousi-Fard, R.; Kamali, O. Enabling ambiguity resolution in CSRS-PPP. *Navigation* **2021**, *68*, 433–451. [CrossRef]
34. Tétreault, P.; Kouba, J.; Héroux, P.; Legree, P. CSRS-PPP: an internet service for GPS user access to the Canadian Spatial Reference Frame. *Geomatica* **2005**, *59*, 17–28.
35. Langley, R.B. Rtk gps. *Gps World* **1998**, *9*, 70–76.
36. Parent, R. *Computer Animation, Algorithms and Techniques*; Elsevier: Amsterdam, The Netherlands, 2012. [CrossRef]
37. Herzfeld, U.C.; Clarke, G.K.C.; Mayer, H.; Greve, R. Derivation of deformation characteristics in fast-moving glaciers. *Comput. Geosci.* **2004**, *30*, 291–302. [CrossRef]
38. Herzfeld, U.C.; McDonald, B.; Stachura, M.; Hale, R.G.; Chen, P.; Trantow, T. Bering Glacier surge 2011: Analysis of laser altimeter data. *Ann. Glaciol.* **2013**, *54*, 158–170. [CrossRef]
39. Herzfeld, U.C. Vario functions of higher order–definition and application to characterization of snow surface roughness. *Comput. Geosci.* **2002**, *28*, 641–660. [CrossRef]
40. Herzfeld, U.C. Master of the obscure—Automated geostatistical classification in presence of complex geophysical processes. *Math. Geosci.* **2008**, *40*, 587–618. [CrossRef]
41. Matheron, G. Principles of geostatistics. *Econ. Geol.* **1963**, *58*, 1246. [CrossRef]
42. Matheron, G. The intrinsic random functions and their applications. *Adv. Appl. Probab.* **1973**, *5*, 439–468. [CrossRef]